Studies on slurry erosion of hard protective coatings on 13-4 martensitic stainless steel for hydro turbine blades

A Dissertation Submitted
in partial fulfilment of the requirements
for the degree of

Master of Engineering
in
Thermal Engineering

by

Gaurav Nath

Registration No.: 801583009

Under the supervision of

Dr. Satish Kumar

Assistant Professor

MECHANICAL ENGINEERING DEPARTMENT

THAPAR UNIVERSITY, PATIALA

June, 2017

CERTIFICATE

I hereby declare that the thesis entitled, **"Studies on slurry erosion of hard protective coatings on 13-4 martensitic stainless steel for hydro turbine blades"** is an authentic record of my work carried out as per requirements for the award of degree of **Master of Engineering** in **Thermal Engineering** at **Thapar University, Patiala** under the supervision of **Dr. Satish Kumar**, Assistant Professor, Mechanical Engineering Department, Thapar University, Patiala during July 2015 to July 2017. No part of the matter embodied in this report has been submitted to any other university or institute for the award of any other degree.

Date: 28 June 2017

Gaurav Nath

It is certified that the above statement made by the student is correct to the best of my knowledge and belief.

Dr. Satish Kumar

Assistant Professor

Mechanical Engineering Department

Thapar University, Patiala - 147004

Dr. Satish Kumar
Assistant Professor
Mechanical Engineering Deptt.
Thapar University, Patiala

Dedicated to

My family

My friends

And

MUSE

Acknowledgements

I would like to express my gratitude to my supervisor **Dr. Satish Kumar**, **Assistant Professor, Mechanical Engineering Department, Thapar University, Patiala** for the useful comments, remarks and engagement throughout the learning process of this master thesis. Furthermore, I would like to thank **Dr. Anjan Sil, Head of Department, Metallurgical and Materials Engineering, IIT Roorkee** for allowing me to use their erosion lab facilities. Also, I would like to thank **Mr. Guru Prakash**, **Research Scholar, Metallurgical and Materials Engineering, IIT Roorkee** for assisting me in my work. I would like to thank my friends and my family, who have supported me throughout entire process, both by keeping me harmonious and helping me putting pieces together. I will be grateful forever for your love.

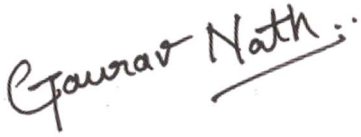

Gaurav Nath

Abstract

Silt erosion is a tenacious hurdle in the efficient operation of hydroelectric plants. The costs involved in repairing the damage done by silt erosion as well as the reduced power output is not favourable. Solution to this problem lies in the use of protective coatings which have proven to be quite effective against silt erosion. Furthermore, predicting the erosion affected areas beforehand using simulations also help to combat silt erosion.

The main aim of this study was to evaluate the slurry erosion resistance of the hard protective coatings used on hydro turbine blades to minimize the damage done by silt erosion. The protective coatings chosen for this study were high velocity oxygen fuel (HVOF) applied 86WC10Co4Cr cermet and boronizing. The most commonly used turbine blade steel 13Cr4Ni martensitic stainless steel (13-4 MSS) was chosen as the substrate for the coatings. An improvement upon the existing 86WC10Co4Cr cermet has also been made by the addition of 2 wt% yttrium oxide (Y_2O_3) into the cermet. A comparative study of the slurry erosion resistance of 13-4 MSS, 86WC10Co4Cr cermet, Y_2O_3 added 86WC10Co4Cr cermet and boronized 13-4 MSS substrate has been made. A slurry pot tester with an abrasive slurry (10 wt% silica sand in water) was used for the wear testing. Coating characterization was done using SEM, EDS and XRD. Hardness and surface roughness of the coatings were also determined. It was found from the study that coated steels exhibited higher wear resistance as compared to the bare steel. Addition of Y_2O_3 also led to an increase in wear resistance over the conventional cermet. Boronized 13-4 MSS was found to have the highest wear resistance.

A CFD simulation has also been done to model the phenomenon of silt erosion in a Pelton turbine nozzle and spear arrangement and Pelton turbine runner. The simulation was done in ANSYS FLUENT using discrete phase modelling (DPM). The eroded areas predicted by simulation were found to be in agreement with the literature and field results. The effect of inlet parameters on the erosion rate was also found to be in agreement with the literature.

Key words: Slurry erosion, 13-4 martensitic stainless steel, HVOF coating, Boronizing, Yttrium oxide, Discrete phase modelling.

Contents

List of Figures

List of Tables

Nomenclature

WC	Tungsten Carbide
Co	Cobalt
Cr	Chromium
Ni	Nickel
Y_2O_3	Yttrium Oxide
SiC	Silicon Carbide
B_4C	Boron Carbide
KBF_4	Potassium Tetrafluoroborate
FeB, Fe_2B	Iron Borides
13-4 MSS	13 Chromium 4 Nickel Martensitic Stainless Steel
WOKA	86WC10Co4Cr cermet
WOKA + Y_2O_3	86WC10Co4Cr cermet + 2 wt% Yttrium Oxide
μm	Micrometer
g/l	Gram per litre
ppm	Parts per million
RPM	Revolutions per minute

Abbreviations

SEM	Scanning Electron Microscopy
EDS	Energy Dispersive Spectroscopy
XRD	X-ray Diffraction
HVOF	High Velocity Oxygen Fuel
CFD	Computational Fluid Dynamics
DPM	Discrete Phase Modelling
UDF	User Defined Functions

Chapter 1

Introduction

Hydropower is one of the most environment friendly sources of energy known to mankind. Hydropower is also a renewable source of energy, which makes its development even more important over fossil fuels and other non-renewable resources. Countries like India, which have a latent potential for hydroelectric power, should invest in this resource to meet their country's enormous energy needs. Although with thermal power still dominating, hydroelectric power only contributes to 26% of the total power generation. Also, despite of the huge hydroelectric potential, only 17% of it has been tapped till date [Ministry of Power, 2008]. Hydropower still faces many challenges in its way. One of those challenges is silt erosion.

During the monsoon season, a large amount of sediment (silt) is swept along with the runoff into the hydro turbines leading to severe damage to the turbine components. Silt is very hard (900 to 1000 VHN) and large concentrations (upto 20,000 ppm) of it can result in erosive wear of hydro turbine components like blades, runners, seals, liners, passages, etc. This can lead to structural failures, leakages, deformation of runner and blades and reduced power outputs [Padhy and Saini, 2008]. All this damage adds to the maintenance and repair cost, and lowers the overall efficiency of the plant. Silt erosion is especially pronounced in the run-of-river type small hydro power stations.

Various approaches are available to curb the damage done by silt erosion. Sedimentation chambers are being used to filter out the large chunks of silt before they enter the hydro turbine. Although, not all the silt can be filtered out. Hard protective coatings and surface treatments like thermally sprayed cermets, plasma nitriding, boronizing, etc. are also being done on the hydro turbine components to make them hard, erosion resistant and to prolong their life. The operating conditions of the hydro turbine and the plant can also be varied to limit the damage caused by silt erosion. Nowadays, cutting edge CFD simulations are being done to predict the effect of silt erosion beforehand and accordingly the design of the turbine is modified to reduce the impact of silt erosion. Knowledge of the erosion prone areas beforehand is very useful in reinforcing said areas with protective coatings.

1.1 Silt erosion

Silt erosion is the erosive wear of hydro turbine components by the hard silt particles which are carried by water and impact the surface leading to material loss. The mechanism of erosive wear may vary depending upon the nature of the surface. In ductile materials, the mechanism of material removal is through repeated plastic deformation followed by cutting whereas in brittle materials, initial crack formation leads to subsequent brittle failure. Also, ductile materials tend to show maximum erosion near low impingement angle while brittle materials tend to show maximum erosion near normal angles of incidence [Hutchings and Shipway, 1992]. Factors affecting silt erosion include - sediment (silt), fluid carrying the sediment and base material. The effect of these parameters on the rate of silt erosion is mentioned below.

1.1.1 Sediment characteristics

A) Size and shape

Rate of erosion generally increases with increase in size of the erodent particle. Particles in the size range above 200 μm are extremely eroding while even finer silt (less than 200 μm) can cause significant wear if supplied under a high head [Padhy and Saini, 2009]. Shape of the silt particles also affects the erosion rate significantly. Angular shaped particles tend to cause more erosion than rounded particles [Padhy et al., 2012].

B) Hardness

Silt consists of quartz, which is very hard (900 to 1000 VHN) and easily erodes softer materials like steel. More the hardness of the erodent particle, more is the rate of erosion.

C) Concentration

Silt concentration in the discharge varies from time to time depending upon factors like rainfall and can reach as much as 20000 ppm. As the concentration of silt in water increases the intensity of erosion also increases. The limiting value of silt concentration to avoid significant damage is shown in Table 1.1 as given by Kumar et al. [2013].

Table 1.1: Limiting value of silt concentration to avoid significant damage for various heads [Kumar et al., 2013].

Type of head	Limiting silt concentration (ppm)
Low and medium head	200
High head	150

1.1.2 Fluid characteristics

A) Velocity

Velocity of the silt particle impinging on a surface is same as the velocity of the fluid medium carrying it. Hence, higher the velocity of the fluid, more is the particle impingement energy and higher is the erosion rate. Although, a limiting value of velocity called the critical velocity is needed to cause some significant wear. Above the critical velocity, the silt particles can easily cut across the surface leading to wear [Patel et al., 2013].

B) Impingement angle

The angle between the path of erodent particle and the target surface is called impingement angle. The effect of impingement angle on the erosion rate depends upon the nature of the target surface as the mechanism of material removal changes accordingly [Hutchings and Shipway, 1992].

C) Temperature

High temperature may soften the target surface making erosion easier and increasing the wear rate [Neopane, 2010].

1.1.3 Base material

Properties of base material like hardness, microstructure, work hardening, etc. significantly affect the rate of erosion. Generally, materials with higher hardness exhibit good wear resistance. Although, too much hardness with no toughness can also lead to failure and subsequent wear. Micro structural defects can also lead to failure and increased wear. Work hardening properties of materials like steels, enables them to harden as they get eroded. As a result, their wear rate falls subsequently on account of work hardening [Hutchings and Shipway, 1992].

1.2 Damage done by silt erosion

In the lower Himalayan region of India, the problem of silt erosion is quite pronounced in the local hydro power plants. The quartz rich silt present in the region is due to the combination of the following factors, steep gradient of water bodies, less vegetation to hold up the soil, severe weather conditions leading to weathering of rocks and also the geological age of the Himalayas. Hydro power plants located in the states of Himachal Pradesh and Uttarakhand like **Bhabha, Malana, Baspa, Maneri Bhali, Baira-Siul, Salal, Dehar,** etc. are the most affected by silt erosion [Swarnakar et al., 2008]. Table 1.2 shows the amount of eroded material each year due to silt erosion in a few hydro power plants in the lower Himalayan region.

Table 1.2: Silt erosion affected hydro power plants in the lower Himalayan region [Kumar et al., 2013].

S.No.	Project	State	Capacity (MW)	Silt particle size (mm)	Eroded Material in kg/year
1.	Nathpa Jhakri	H.P.	6×250	0.22	3438
2.	Bairasiul	H.P.	3×60	0.24	4143
3.	Maneri Bhali-I	U.K.	3×30	0.25	3324
4.	ManeriBhali-II	U.K.	3×9+2×4	0.23	2488
5.	Dehar	H.P.	6×165	0.26	6588
6.	Giri	H.P.	2×30	0.35	7420

In Pelton turbines, the most affected areas include **inlet passages, nozzle/spear governing assembly, turbine runner and the wheel pit.** The main reason for erosion in Pelton turbines being the very high velocities of particles in the jet (approx. 100 m/s) impacting the runner. In Francis turbines, the most affected areas include **inlet passages, guide vanes, runners and labyrinth seals, draft tubes, and shaft seals.** Francis turbine being a reaction turbine, the guide vanes converts approximately fifty percent of inlet energy into kinetic energy while the rest remains in the form of pressure energy. Hence, guide vanes and inlet of the runner are subjected to a high absolute velocity [Brekke et al., 2002]. Figures 1.1 and 1.2 show the silt erosion affected areas in Pelton and Francis turbines.

(a) Nozzle needle, Mel, Norway

(b) Splitter, Rangjung, Bhutan

Figure 1.1: Silt erosion damage in Pelton turbine components (a) Nozzle needle, Mel, Norway (b) Splitter, Rangjung, Bhutan [Neopane et al., 2011].

(a) Eroded guide vanes

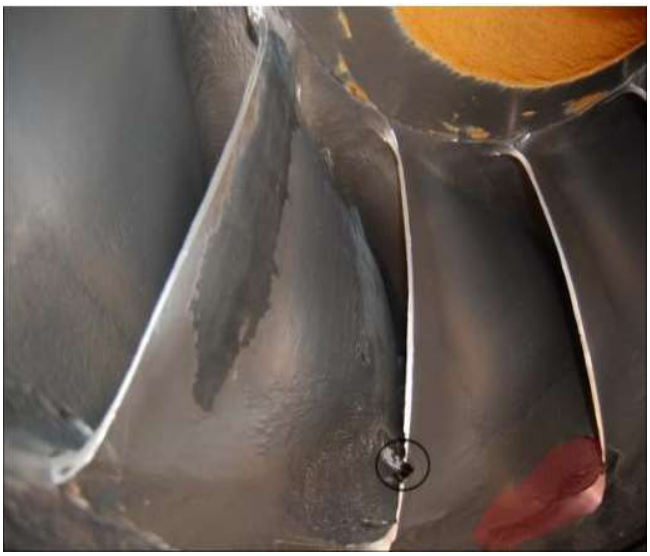

(b) Eroded runner blade

Figure 1.2: Silt erosion damage in Francis turbine components (a) Eroded guide vanes (b) Eroded runner blade at Cahua power plant [Neopane et al., 2011].

1.3 Protective coatings

Protective coatings are one of the most useful defense measures against silt erosion. Protective coatings are applied on the hydro turbine components like runner blades, guide vanes, seals etc. These protective coatings being quite hard provide superior wear resistance against silt erosion and help to prolong the lives of the components. A variety of protective coatings and surface treatments are available -

- Thermally sprayed (HVOF or D-gun) WC-Co-Cr/WC-Co cermet coatings.
- Plasma nitriding
- Boronizing
- Chrome plating

1.3.1 High velocity oxygen fuel (HVOF) applied WC-Co-Cr cermet

WC-Co-Cr cermet and its variations are the most widely used and commercially successful hard coatings that are applied on hydro turbine components to protect them from erosion and restore damaged parts. A cermet is a composite material comprising of one-part ceramic (cer) and the other part a metal (met). It has the best properties of both a ceramic and a metal. It possesses the high hardness and melting point of a ceramic while retaining the ductility and toughness of a metal. The metal part is used as a binder for the hard ceramic reinforcement and to provide some degree of toughness. Cermets can also be in the form of metal matrix composites, where a hard ceramic is dispersed in a metal matrix [Callister, 2011]. An example is the 86WC10Co4Cr cermet, in which tungsten carbide ceramic is dispersed in cobalt chromium metal matrix. The hardness of the ceramic phase combined with the toughness of the metal phase make the cermet a very good erosion resistant coating.

WC-Co-Cr cermet is usually thermally applied via HVOF process. In the HVOF process, fuel in the form of either a gas (hydrogen, propylene, propane, acetylene) or a liquid (kerosene) is fed into the combustion chamber along with oxygen. Figure 1.3 shows the construction of a HVOF spray gun. An ignition starts the combustion process and the high temperature exhaust gases rush out through a nozzle and towards the target at a very high speed. The entire gun is cooled by water. The extremely high volume of the exhaust gases, along with the high temperature of combustion (5500 K), produces jet velocities in the range of 1525 to 1825 m/s at

the nozzle exit [Davis, 2004]. Powders to be coated are transported via a carrier gas into the exhaust gas jet either radially or along the axis, where they become entrained into the high temperature/velocity jet of gases and reach a velocity of 200 to 1000 m/s [Davis, 2004]. These particles in the molten or semi molten state, strike the surface of the substrate at a very high speed forming strong mechanical inter-locking with the substrate.

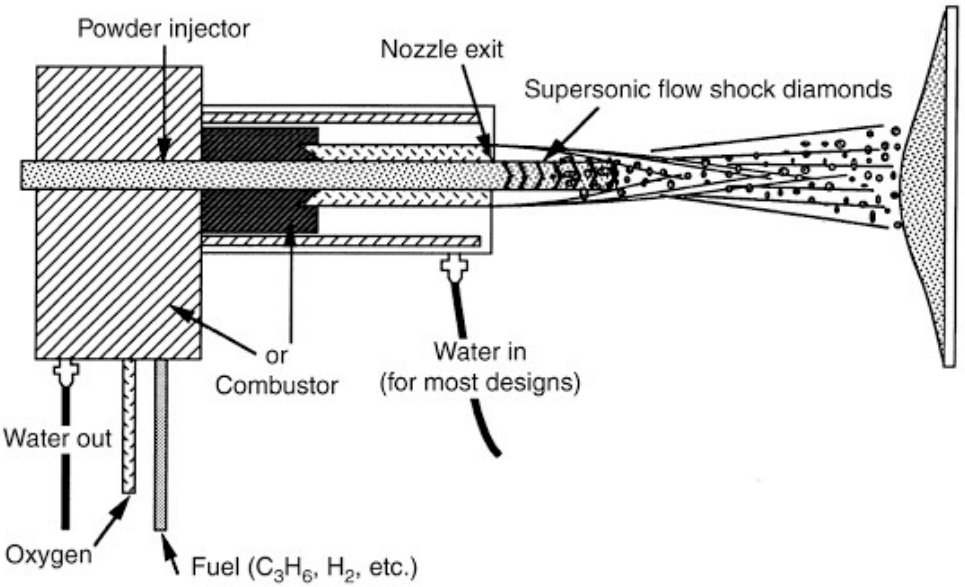

Figure 1.3: Schematic of a HVOF gun [Davis, 2004].

As compared to other modes of thermal spraying like flame spraying or plasma spray, the particle velocities achieved in HVOF is more which subsequently leads to denser coatings and strong adhesion. Also, average temperature of the particles in HVOF is lower than the other methods, which in turn reduces the degree of oxidation and decomposition of the particles. Even with the lower particle temperatures, the density of coatings applied via HVOF is still very high on account of the high particle impact velocities [Davis, 2004]. HVOF-sprayed carbide composites have very high tensile bond strengths (as much as 90 MPa). HVOF-sprayed coatings have a porosity of less than 1%. HVOF applied coatings usually fall in the thickness range of 100 to 300 μm [Pawloski, 2008].

1.3.2 Boronizing

Apart from thermal spray coatings, surface hardening processes like boronizing can also be used to effectively reduce wear of components. Boronizing is a thermo-chemical process which involves diffusing boron into the surface of the substrate. The procedure includes, diffusing boron atoms into the lattice of the substrate metal (Iron) using thermal energy to form iron borides (Fe_2B and FeB) [Fichtl, 1981]. The formation of these extremely hard borides on the surface increases the wear resistance of bare steel substrate many times.

The source of boron required for the diffusion can either be gaseous, liquid or a solid. The limitation with the gaseous method is the requirement of complex and expensive equipment and the toxic nature of the source (Diborane). Liquid boronizing has technical limitations regarding the immersion of the substrate in the liquid boron source as well as the formation of FeB + Fe_2B. FeB is not desirable from wear point of view owing to its brittleness [Fichtl, 1981]. Solid state boronizing is generally preferred instead. Solid boron carbide is used as the source of boron. Although, many variations of the process exist, the pack boronizing method being the easiest is discussed here.

Pack boronizing is a solid state process, which means that there is no melting involved. A mixture consisting of a boron source (usually boron carbide), an activator (e.g. potassium tetrafluoroborate or ammonium bifluoride) and an inert material (like silicon carbide) is made and mixed thoroughly. The mixture along with the component to be coated is placed in a steel box. The box is then heated to a temperature of 930±5˚C and held for 6 hrs. The samples are then either furnace cooled or oil quenched [Mann, 2000].

Boronizing has been used successfully in many industries mainly for the purpose of improving the wear resistance and prolonging the life of the components. Boronizing has been used in textile industry to coat machine parts, in the chemical industry for pneumatic conveying parts like bends, in industrial oil firing for coating nozzles and injectors, in coating dies, suspensions for railway carriages, in automobile industry for high performance of engine parts, etc. [Fichtl, 1981]. Although, there is not much information about the application of boronizing in hydro turbine components, it has been suggested that it is a viable option. Owing to its high hardness (1600 to 2000 VHN), it can be used for coating hydro turbine components subjected to high energy particle impingement (more than 5 μJ) [Mann, 2000].

1.4 Use of computational fluid dynamics (CFD)

Apart from the experimental approach, a theoretical/numerical approach can also be useful against silt erosion. Nowadays, commercial software packages like ANSYS FLUENT, OPENFOAM, etc. enable engineers to simulate complex fluid flow through various structures and turbo-machinery. These software use a numerical approach to solve the governing equations of conservation of mass, momentum and energy over a discretized domain. Not only basic fluid flows, flows involving a mixture of a number of phases including solid, liquid and gases can also be modelled using multiphase flow models. Many models are recommended based on the mixture of phases. For simulating silt erosion, liquid water along with solid silt particles need to be modelled. Discrete phase modelling (DPM) is used most commonly for such applications. Such simulations can help to predict the regions which are most susceptible to erosion.

1.4.1 Discrete phase modelling (DPM)

For simulating multiphase flows, two approaches are commonly used. In the Euler-Lagrangian approach, the continuous phase is treated in the Eulerian frame of reference and the discrete phase is treated in the Lagrangian frame of reference. While in the other approach, both the phases are treated in the Eulerian frame of reference. For simulating erosion related problems, where the volume fraction of the discrete phase is small as compared to the continuous phase, the Euler-Lagrangian approach is used. The DPM model handles the Lagrangian treatment of the particles and is used for simulating the silt. The mechanism of a DPM solver is described as follows. Based on the user input conditions of the discrete particles, the particle trajectories and the heat/mass transfer calculations are initiated. The continuous phase is solved and after a user defined number of continuous phase iterations, a DPM iteration takes place. In the DPM iteration, the particle trajectory and the heat/mass transfer equations are recalculated based on the surrounding local continuous phase. The particle trajectory equation [ANSYS Inc., 2009] is given in Eq. (1.1).

$$\frac{du_p}{dt} = F_D\left(u - u_p\right) + \frac{g_x\left(\rho_p - \rho\right)}{\rho_p} + F_x \tag{1.1}$$

where

u is the fluid phase velocity

u_p is the particle velocity,

ρ is the fluid density,

ρ_p is the density of particle

$F_D(u - u_p)$ is the drag force per unit particle mass

$\frac{g_x(\rho_p - \rho)}{\rho_p}$ is the gravity force

F_x are additional forces: Pressure gradient, etc.

The particle trajectory equation is a force balance equation with the change of momentum of the particle on one side of the equation and forces (drag, gravity, external) acting on the particle on the other side. The particle trajectory, heat/mass transfer equations are solved by stepwise integration over discrete time steps. For example, integrating Eq. (1.1) with time gives the particle velocity and then the following equation can be used for predicting the trajectory shown in Eq. (1.2).

$$\frac{dx}{dt} = u_p \tag{1.2}$$

DPM solver also supports two way coupling between the phases. In one-way coupling, only the fluid phase can affect the particle phase through drag and turbulence. In two-way coupling, not only the one-way coupling is valid, but the particle phase can also affect the fluid phase through mass, momentum and energy transfer. The calculations continue with both the phases affecting each other till a converged solution is obtained. Figure 1.4 shows the mechanism of a DPM simulation [ANSYS Inc., 2009].

DPM model also has several limitations. It is only valid for cases where the volume fraction of the discrete phase doesn't exceed 10% although mass fractions can be large. Particle to particle interactions are also neglected.

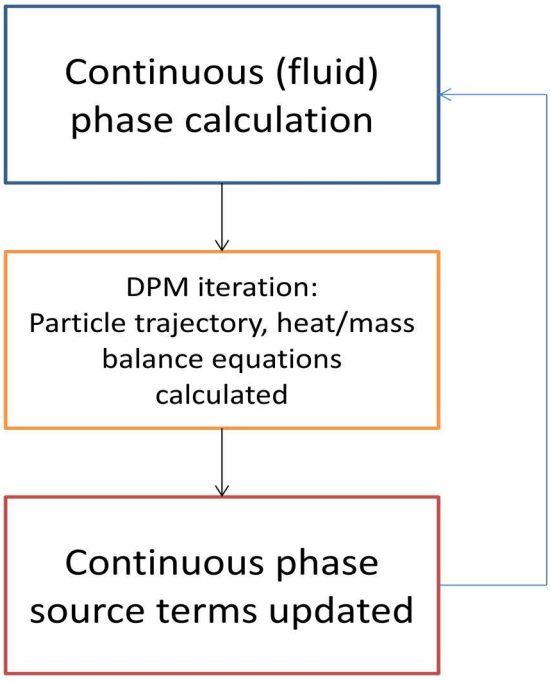

Figure 1.4: Mechanism of DPM simulation [ANSYS Inc., 2009].

1.4.2 Erosion Model

DPM model helps to predict the trajectories of the solid silt particles through the fluid. DPM model also takes into account the reflection/collision when a particle hits a wall. The angle and the velocity of the particle at such an event is recorded which later helps to calculate the erosion at that spot. A theoretical erosion model is used for that purpose. Some of the common examples are Finnie's model, Bitter's model, Tulsa angle dependent model, etc. ANSYS FLUENT uses the following erosion model -

$$R_{erosion} = \sum_{p=1}^{N_{particles}} \frac{m_p C(d_p) f(\alpha) v^{b(v)}}{A_{face}} \tag{1.3}$$

where

$R_{erosion}$ is the erosion rate (kg/m^2-s)

$C(d_p)$ is a function of particle diameter

α is the impact angle of the particle path with the wall face

$f(\alpha)$ is a function of impact angle

v is the relative particle velocity

$b(v)$ is a function of relative particle velocity

m_p is particle mass

A_{face} is face area

The functions and constants used in the above erosion model depend upon the properties of the eroding particle and the target surface.

Chapter 2

Literature Review

2.1 Silt erosion evaluation

Many researchers have evaluated silt erosion and the parameters affecting it either thorough experimentation or by collecting data from the silt affected hydro power plants. Their work and findings have been briefly summarized below-

Padhy and Saini [2009] studied the effect of silt size, concentration and jet velocity on a model Pelton turbine. Wear rate on the buckets were monitored and correlations were developed between the wear rate and the selected parameters. An in-house test rig was built with a 16 bucket brass Pelton turbine, 1 cm jet diameter, 14.4 cm pitch circle dia. Silt concentrations used were 5000, 7500 and 10000 ppm. Four different silt size ranges were used < 90 μm, 90 μm to 180 μm, 180 μm to 250 μm and 250 μm to 355 μm. Jet velocities used included 26, 28, 29 m/s. It was reported that the bucket splitter was found to be the most eroded area. It was also observed that erosion rate increases with increase in silt concentration but the increase in erosion rate is different for different size ranges. The erosion rate also increases with increase in silt size independent of concentration, although the increase in erosion is more pronounced at higher concentrations. Also, erosion rate was also found to increase with jet velocity. Based on all the observations, a correlation was developed linking the erosion rate to the experimental parameters using regression analysis.

Neopane et al. [2011] identified the components which are most severely affected by silt erosion in Pelton and Francis turbines, based on observations from the Cahua power plant in Peru. Guidelines were also suggested as to reduce the effect of silt erosion in hydraulic turbines. In Pelton turbine, the high velocity and acceleration of the silt particles in the jet and at the buckets was found to be the main reason for erosion. The inlet system is moderately affected owing to low velocities. While the nozzle system (needle and ring) and buckets are severely affected. It was suggested that using minimum number of jets, large radius of curvature where flow changes

direction and large hydraulic radius of bucket and nozzle may help curb silt erosion. In Francis turbines, the most severely affected areas include the guide vanes, runner and seals. Based on the observations, the authors suggested the use of a turbine with lower water velocities, lower specific speed, more thickness of blades at erosion prone areas, use of variable speed and selection of proper material to minimize the damage done by silt erosion.

Khurana et al. [2012] studied the effect of nozzle angle and other silt parameters on the erosion rate of a Turgo impulse turbine. For experimental purpose, a brass Turgo impulse turbine was fabricated with 19 blades, 216 mm runner diameter, 12.5 mm nozzle diameter and 1100 RPM speed. Silt particles of sizes 100, 200, 300 and 370 μm, concentrations 3000, 6000 and 9000 ppm and jet velocity of 28 m/s was used for the test. Three different nozzle angles of 20°, 25° and 30° were used. Power output from the turbine was also monitored by coupling a generator with the turbine. It was reported that maximum erosion was observed at 20° irrespective of the silt size and concentration used. This was attributed to the fact that ductile materials exhibit maximum material loss at lower angles due to micro cutting. Erosion rate was observed to decrease at 25 degrees and then again increase at 30° due to the mechanism of material removal changing from micro cutting to impact erosion. Also, loss in efficiency was found to be maximum at 20°.

Thapa et al. [2012] proposed a new empirical model to predict the erosion rates and the corresponding reduction in efficiency of a Francis turbine due to silt erosion. Data for the empirical modelling was collected from Jhimruk Hydroelectric Centre (JHC). Data collected included – particle size distribution, sediment concentrations between the months of September and October, silt composition and reduction in plant efficiency. Two existing erosion models – Bajracharya and IEC (International Electrotechnical Commission) were also evaluated by comparing with actual field results. Results of the IEC model were in better agreement with the field results as compared to the Bajracharya model. Limitation of the Bajracharya model was reported to be its reliance solely on the silt particle size. The new empirical model proposed predicted both the erosion rate and the reduction in efficiency for the Francis turbine. This model predicted a 1% reduction in efficiency of the runner per year, which was found to be in accordance with the field results.

Kumar et al. [2013] developed an empirical model for silt erosion using multivariate nonlinear regression method. The methodology involved collecting data from the 12 most silt erosion affected power plants. The power plants selected were mainly from the north Indian region (Himachal Pradesh and Uttarakhand) like Nathpa Jhakri, Maneri Bhali, Dehar, etc. Next step was determining the factors that significantly affected erosion rate. Factors chosen included silt concentration, velocity and diameter. The model correlated these parameters with the material loss per year. Calculations were done to determine the total material eroded in a year as well as the total silt concentration in tons. The data was then put into the regression model to find a good fit. Microsoft Excel was used for carrying out the regression analysis. The correlation formed was found to be good because of a high R square value (close to 1). The model was validated using data from three more power plants in the lower Himalayan region. The errors were found to be within reasonable limits. Hence, the model was successful in predicting the material loss per year.

Khurana and Goel [2014] studied the effect of jet diameter on the erosion of a Turgo impulse turbine. A custom rig was made for experimental purposes. It consisted of a brass Turgo impulse turbine with 19 blades and 216 mm runner diameter. Three nozzle diameters were used for the test 12.5, 8.8 and 7.2 mm. Silt sizes of 100, 200, 300 and 370 μm and concentrations of 1000, 3000, 5000 and 8000 ppm were used for the test. To maintain a constant discharge, 2 and 3 jets were used with 8.8 mm and 7.2 mm jet diameters respectively while a single jet was used for 12.5 mm jet dia. It was reported that wear increased with increase in silt size and concentration. Also, it was observed that erosion increased with increase in jet diameter independent of the silt conditions. Based on the experimental data, a correlation was formed between the normalized erosion rate and the silt parameters. Comparison with experimental data showed a deviation of about 8%.

2.2 HVOF protective coatings

Protective coatings are one of the most widely used methods of combating erosion. The work done by researchers on HVOF related hydro turbine protective coatings has been summarized below-

Mann [1999] investigated the wear resistance of a variety of coatings and surface treatments for hydro turbine steels in regard to high energy particle impingement (> 5μJ). WC12Co detonation gun sprayed coating, chrome plating, boronizing and plasma nitriding were applied on 13Cr4Ni turbine blade steel. Additionally, boronizing of T410 steel was also carried out. Wear testing was carried out in a custom built facility using sand of avg. size 135 μm and concentration varying upto 10,000 ppm. In terms of hardness, boronized T410 steel came out on the top. Among the 13Cr4Ni coatings, boronizing had the maximum hardness followed by WC12Co coating, plasma nitriding and chrome plating in that order. Results of wear testing revealed that boronized T410 steel exhibited the least amount of wear on account of its high hardness. In the 13Cr4Ni steel, WC12Co showed the best wear resistance despite having lower hardness than the boronized one. This was attributed to the micro structural defects in the boronized 13Cr4Ni steel. Chrome plating and plasma nitriding did not show much significant improvement in wear resistance.

Mann and Arya [2001] investigated the abrasive and erosive wear resistance of HVOF sprayed WC-10Co-5Cr and plasma nitriding on common hydro turbine steels like 13Cr4Ni and 12Cr. HVOF coatings were deposited using a Met Jet II HVOF system. Use of plasma nitriding over conventional nitriding resulted in a much superior quality coating. Erosive wear tests were done in a custom rig using 1100 VHN silt and 2350 ppm silt concentration. Abrasive wear resistance test was done using the ASTM G-65 standard. It was found that the HVOF coating had the highest hardness followed by plasma nitriding. Bare steel had the lowest hardness. Wear testing results revealed that both HVOF and plasma nitriding showed much better abrasive and erosive wear resistance than the bare steel. HVOF coating outperformed plasma nitriding owing to its higher hardness. Although, SEM examination revealed defects (voids) in the HVOF coating while no such defects were found in plasma nitrided steels.

Machio et al. [2004] studied the abrasive and slurry erosion resistance of HVOF sprayed WC-VC-Co coatings. The conventional coatings WC-12Co and WC-17Co were modified by replacing some percentage of tungsten carbide with vanadium carbide (VC) leading to the modified coatings WC-10VC-12Co and WC-10VC-17Co. Coatings were deposited via JP 5000^{TM} HVOF system on stainless steel substrates. Abrasion testing was done in accordance

with ASTM G65-85. For the slurry tests, 5 wt% abrasive slurry jet was impinged at a velocity of 12.6 m/s. It was found that the addition of VC reduced the hardness of the coatings. Also, the addition of VC improved the abrasive wear resistance of the coatings, which was attributed to the fact that coatings with VC showed less binder removal. Although, in slurry erosion tests, no significant difference in wear performance was obtained.

Maiti et al. [2007] added additional WC powder (10%, 20% and 30% by wt.) to the existing WC-9Co-5Cr cermet and studied their abrasion and slurry erosion resistance. The new coatings were then deposited on mild steel substrates using Metjet-III kerosene based HVOF system. Abrasion and slurry erosion tests were performed using ASTM G-65 and G-73 standards respectively. It was found that addition of WC resulted in increased hardness of the coatings with the hardness progressively increasing with the additional WC content. Although, despite of the higher hardness of the coatings, a decrease in wear performance of the coatings is observed in both abrasion and slurry erosion tests. The performance was found to degrade with increase in the WC content. On SEM examination of the coatings it was found that, the porosity increased with the increase in WC content. The increased porosity of the coatings was stated as the reason for the poor wear performance.

Goyal et al. [2012] studied the slurry erosion resistance of HVOF applied WC10Co4Cr and Al_2O_3 + TiO_2 coatings on CF8M turbine steel. The effect of particle size, speed and slurry concentration on the wear performance was also studied. The erosion tests were carried out in a high speed slurry erosion tester (Ducom TR401) using silt from the Nathpa Jakhri plant in Himachal Pradesh. For studying the effect of parameters, two particle sizes 100 µm and 300 µm, concentrations 10,000 ppm and 30,000 ppm and speeds 2250 and 4500 RPM were used. Results showed that WC10Co4Cr showed much better wear resistance than Al_2O_3 + TiO_2 owing to its higher hardness. Speed of rotation was observed to be a significant factor affecting the erosion rate for all samples. While particle size was found to be significant in Al_2O_3 + TiO_2 coating, same was the effect of slurry concentration on the uncoated steel. Mechanism of erosion was found to be ductile for the CF8M steel, mixture of ductile and brittle for WC10Co4Cr and mainly brittle for Al_2O_3 + TiO_2 coatings.

Thakur and Arora [2017] added multi-walled carbon nanotubes (CNT) into nano WC10Co4Cr cermet in an attempt to improve the binder strength and improve erosion resistance. Slurry erosion behaviour of the micro cermet, nano cermet and CNT added nano cermet was studied. Coatings were deposited using JP-5000 HVOF system. A jet type erosion tester was used with impingement angles of 30˚ and 90˚. It was observed that the nano coatings performed much better than the micro coating when it comes to slurry erosion resistance. This was attributed to the fact that less binder material was removed from the nano coatings. At 30˚, the wear mechanism was found to be the micro cutting of the binder matrix leading to pulling out of the WC grains. At 90˚, the wear mechanism was found to be the fracturing of WC grains leading to exposed binder matrix. Also, CNT added nano cermet exhibited better wear resistance as compared to the original nano cermet. It was found that the addition of CNT in the cermet improved the fracture toughness of the coating.

2.3 Boronizing of steel

Work done by researchers regarding boronizing of steel, its erosion, process parameters and applications has been summarized below -

Subrahmanyam [1982] did the boronizing of mild steel using pack cementation technique and investigated the effect of varying the process temperature and the amount of activator in the boronizing mixture. For pack boronizing, boron carbide was used as source with ammonium bifluoride as activator. The composition of activator was varied (1% and 2%) to make two different boronizing mixtures and to study their effect. Similarly, two process temperatures (900˚C and 1000˚C) were also chosen. At low temperature (900˚C) and 1% activator, FeB+Fe_2B phase is formed. At high temperature (1000˚C) and 2% activator, also two phase FeB+Fe_2B is formed. At high temperature (1000˚C) and 1% activator, only FeB is formed. At low temperature (900˚C) and 2% activator, only Fe_2B is formed. In the two phase coatings, FeB is formed on the surface with Fe_2B layer below it. The microstructure also shows the characteristic finger like extensions between the boride layer and the steel substrate. Hence, depending upon the temperature during boronizing and activator amount, different phases can be formed in the coating.

Subrahmanyam and Gopinath [1984] conducted pin on disc type sliding wear tests on boronized mild steel samples containing single phase FeB, Fe_2B and two phase FeB + Fe_2B. The tests were conducted under dry and unlubricated conditions on high carbon tool steel disc. Boronized layers with different phases were produced on mild steel samples by varying the process temperature and activator amount. It was observed that single phase coatings like FeB and Fe_2B exhibited better wear resistance than the two phase FeB + Fe_2B. It was attributed to the inhomogeneity of the two phase coating. The wear debris was studied for each case. It was also reported that in dual phase borides, the wear mechanism was the adhesion and transfer of the oxidized particles. Wear mechanism for the single phase FeB layer, was abrasion and removal of oxidized particles. For Fe_2B layer, fatigue and oxidation of the particles was the main cause of wear.

Mann [1996] studied the abrasion and cavitation erosion of boronized 13Cr4Ni martensitic stainless steel (13-4 MSS) commonly used in hydro machinery. Boronizing of steel has proved to increase the abrasive and adhesive resistance several times, but the study was conducted because of a lack of information on boronizing of 13-4 MSS. The boronizing was done using pack boronizing, which is a solid state process with no melting. 5% boron carbide (boron source) along with 2% ammonium bifluoride (an activator) and 93% silicon carbide (inert agent) were placed along with a steel sample in a container and heated to 930˚C for 6 hours and then furnace cooled. Some of the samples were also given a post tempering heat treatment. A rotating disc apparatus was used for the cavitation erosion test. A rubber wheel apparatus with dry sand was used for the abrasion test. Boronized 13-4 MSS exhibited poor cavitation erosion resistance because of its brittle structure, whereas abrasion resistance improved due to increased hardness. Tempering heat treatment led to some improvements against cavitation erosion but reduced the abrasion resistance due to reduction in hardness.

Sundararajan and Jain [2002] investigated the optimum thickness of the boronizing mixture required for the pack boronizing of low carbon steel samples without compromising the properties of the boride coating. This study was done in an effort to bring down the cost of boronizing process by using only the optimum amount of boronizing mixture. Instead of the commercial boronizing mixture consisting of boron carbide source, KBF_4 activator and silicon

carbide, a new patented mixture (LABM) was used with low born activity. ASTM G-65 standard was used for the rubber wheel abrasion test. It was reported that the thickness of 10 mm was found to be optimum for boronizing low carbon steel samples at 940˚C for 2 hrs. For smaller pack thickness, a smaller boride layer is observed which is likely due to deficiency of the boron source. The higher abrasive wear rates in samples with lower pack thickness can be explained by the presence of oxides present in them. These oxides were absent in samples with pack thickness greater than or equal to 10 mm.

Joshi and Hosmani [2014] did pack boronizing of AISI 4140 steel and studied the effect of size of the mild steel container used for boronizing on the formation of various phases in the boronized layer. Three sizes of the container were used small sized, medium sized and big sized. Boronizing of the containers was also done beforehand as it was observed that non-boronized containers exhausted the boron source leading to poor quality coatings. It was reported that the steel samples failed to boronize in the small sized container while they did in the medium and big sized containers. Also, it was observed that use of big sized containers resulted in the formation of Fe_2B + FeB layer out of which is FeB is undesirable. Although medium sized container was found to produce Fe_2B layer consistently. A pin on disc sliding wear test was also conducted. Boronized steel exhibited much better wear resistance as compared to the bare steel because of its higher hardness.

2.4 CFD modelling of silt erosion

The work done by researchers in simulating the silt erosion phenomenon using CFD has been summarized below –

Mack et al. [1999] used a numerical approach to determine the erosion in the labyrinth seals and guide vanes of a Francis turbine. The Lagrangian treatment of particles was used for simulating erosion. k-ϵ model was used for the fluid flow. Finnie's model was used for calculating the erosion rate. Enlargement of labyrinth seals was reported as the cause for leakages and reduction in efficiency of the turbine. Field results were used to validate the flow through the simulated 2D labyrinth. Two sizes of silt particles 15 μm and 200 μm were used for the simulation. It was observed that larger sized particles caused more erosion than the smaller particles on the

labyrinth walls. The erosion predicted on the first and second gap of the seals by the simulation was found to be in agreement with the field observations. A 3D simulation was done for the guide vanes. Three particle sizes 30 μm, 60 μm and 80 μm were used for the guide vane simulation. Except for the region near the leading edge (about 30%), remaining portion of the pressure side of the vane showed heavy erosion. Similarly, on the suction side, heavy erosion was predicted on the trailing edge. The predicted erosion patterns were found to be in good agreement with the field tests.

Campos-Amezcua et al. [2007] did a CFD simulation of solid particle erosion using DPM in a 300 MW steam turbine nozzle. Standard k-ϵ model was used. Mesh independence was also achieved. For the boundary conditions, a rotational periodic type condition was used. Erosion contour plot revealed that the most eroded region is the trailing edge. Erosion in leading edge was found to be less as compared to the trailing edge. Effect of varying steam mass flow rate, solid mass flow rate, and particle diameter on erosion rate was also studied. Erosion rate was found to decrease with reduction in steam flow rate as particle velocities also diminish. Increase in the solid particle mass flow rate lead to increase in the erosion rate, as expected. When particle diameter was increased, the erosion rate was found to decrease as the number of particles reduced for a given mass flow rate.

Wilson et al. [2011] developed a CFD model to capture the combined effect of erosion and corrosion in a pipe bend geometry to account for the huge wastage losses in the oil industry. Discrete phase modelling (DPM) was used in Fluent to simulate the erosion phenomenon in a pipe bend using different erosion models. The erosion models used were Finnie's, Sundararajan, Nielson and Gilchrist's and Forder's. It was reported that FLUENT's erosion models greatly under predict erosion as compared to experimentally verified data, reporting approximately one third of the true erosion in most cases. The effect of varying the flow velocity and particle shape on the erosion rates predicted by models were also compared. A UDF was used to combine the erosion model with corrosion model and display the combined effects on the pipe bend. Erosion-corrosion regimes ranging from erosion dominated, mixed and corrosion dominated were suggested by Wilson et al. Results of the simulation showed the various erosion-corrosion

regimes on the pipe bend at different temperatures. Erosion dissolution and plain erosion were found to be the major reasons for material wastage.

Chongji et al. [2014] conducted a 3D multiphase unsteady simulation of water, silt and air through a Pelton turbine nozzle. For fluid flow, RNG k-ϵ model was used. DPM model was used for the modelling the silt particles and VOF (Volume of fluid) model was used to model the interaction between air and water. The simulation predicted the velocity and pressure distributions at the nozzle opening and the jet. Velocity was found to increase along the needle while the pressure was found to decrease till the nozzle tip followed by an increase. Silt particles were introduced in the simulation after water-air simulation stabilized. It was observed that the needle base and tip were found to be the most eroded regions. On comparison with the field observational results, it was found that the erosion at the needle base was a bit over predicted. The erosion at the needle tip was found to be consistent with real world results.

Kumar and Saini [2015] simulated the phenomenon of silt erosion in a Pelton turbine runner and evaluated the mass loss in Pelton buckets. The simulation was carried out in Fluent using DPM modelling under varying conditions of silt size, shape, concentration and jet velocity. The geometry of a 20 bucket, single jet, 1.5 MW Pelton turbine was modelled for the simulation. Standard k-ϵ model was used for the fluid flow with DPM model being used for the silt. The runner was also given rotatory motion (400 RPM) using mesh motion. Results of the fluid flow simulation revealed that the operating characteristics of the simulated turbine and actual turbine deviate by a max. of 4.7%. Results of the silt flow simulation revealed the splitter of the bucket to be the most eroded area. Also, a deviation of 21% was observed between the simulated and actual results for the normalized wear rates. Wear was also found to increase with silt size, concentration and jet velocity. Silt with shape factor of 0.5 was found to be the most eroding.

Sangal et al. [2016] did a CFD simulation to study the effect of silt erosion on the efficiency of a Kaplan turbine and also predict the areas affected by erosion. The simulation was carried out in ANSYS 14.0 using SST k-ω model for turbulence and DPM model for silt particles. A 3D model of the Kaplan turbine with 15 wicket gates and 5 runner blades was designed in Pro-E CAD software. A tetrahedral mesh was generated on the geometry. For the boundary conditions,

different wicket gate openings 60%, 80%, 100% and 110% were modelled. Simulation with only fluid flow revealed the best efficiency of turbine at 80% gate opening with minimum losses. It was also reported that the runner and draft tube affect the efficiency of the turbine significantly. For silt flow, silt sizes 0.005, 0.01, 0.05 and 0.1 mm and concentrations 5000, 7500 and 10000 ppm were used. It was observed that the blade tips and trailing edge were the most eroded areas. It was also reported that reduction in turbine efficiency is higher at best efficiency point with the silt flow.

2.5 Gaps in literature

1. Since, the erosive wear phenomenon is not well understood, there is lack of a complete and standardized erosion model for it.
2. Experimental slurry erosion studies have been confined to erodent particles of the same size. Only a few researchers have taken into account the particle size distributions of the silt present in the discharge of actual hydro power plants.
3. Similarly, the variation in silt concentrations throughout the year has not been taken into account in many experimental studies.
4. The empirical correlations for erosive wear in terms of silt parameters, developed by curve fitting the experimental data may not be applicable for all situations. This is due to the fact that the data used for the regression analysis is taken from a limited number of cases.
5. Experimental test rigs developed by different researchers show large deviations in results due to the lack of a proper standard, as well as the difficulties in controlling the parameters responsible for erosive wear.
6. Not much work has been done on HVOF coatings on martensitic stainless steel (13-4) especially those used in hydro turbines.
7. Also, the WC/Co-Cr cermet chosen for the hydro turbine coatings has practically remained the same over the years with little to no modifications. It is being widely used with no other significant variants.
8. Boronizing has been successfully applied to reduce wear in many applications. However, there is not much information on its use in hydro turbine components to reduce erosive wear.
9. Abrasive and sliding wear behaviour of boronized steels have been extensively studied with little work on the erosive/slurry wear behaviour.

10. Most researchers rely on Eulerian-Lagrangian methodology i.e. continuous phase simulation + DPM for predicting silt erosion in hydro turbines. However, cavitation and corrosion are also responsible for erosion in hydro turbines. There is lack of a complete model that combines the effect of particle erosion, cavitation and corrosion.
11. Finnie's theoretical model for wear is being used by most researchers in simulations, while it has been known to over predict wear in many situations. Little work has been done using other erosion models.

2.6 Objectives

1. To study the slurry wear resistance of HVOF applied WC10Co4Cr cermet coating on 13-4 martensitic stainless steel being currently used for hydro turbines.
2. To improve the wear resistance of the WC10Co4Cr cermet coating by the addition of another hard phase - 2 wt% yttrium oxide (Y_2O_3).
3. To study the slurry wear resistance of pack boronized 13-4 martensitic stainless steel.
4. To model the silt erosion phenomenon in a Pelton turbine using discrete phase modelling and predict the erosion prone areas.

Chapter 3

Coatings, Characterization and Experimental Setup

3.1 Substrate

13Cr4Ni martensitic stainless steel (13-4 MSS) was used as substrate for the HVOF coatings and boronizing. It was procured from BHEL, Haridwar. Its composition is mentioned in Table 3.1. 20 mm × 20 mm × 6 mm samples of 13-4 MSS were cut and prepared for coatings (Fig. 3.1).

Table 3.1: Nominal composition by wt. of 13Cr4Ni martensitic stainless steel.

C	Si	Mn	P	S	Cr	Ni	Mo	Fe
0.0646%	0.6261%	0.3833%	0.0113%	0.0256%	13.35%	3.240%	0.4078%	Balance

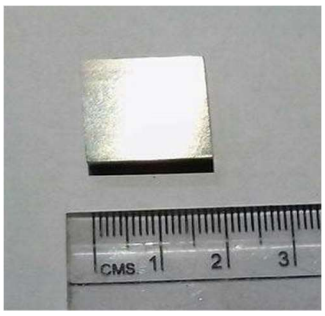

Figure 3.1: 13-4 MSS sample.

3.2 HVOF coatings

The following two cermets were chosen to be applied on the 13-4 MSS via HVOF method –

3.2.1 Tungsten carbide in cobalt-chromium matrix (86WC10Co4Cr)

This cermet coating is widely used and is commercially available (WOKA 3652 FC manufactured by Oerlikon Metco). This cermet was procured from Oerlikon Metco in the form of an agglomerated and sintered powder with spheroidal morphology. Properties and

composition of WOKA 3652 FC are shown in Table 3.2. In this cermet, tungsten carbide acts as hard reinforcement while cobalt-chromium matrix provides toughness and acts as binder.

Table 3.2: Properties of 86WC10Co4Cr (WOKA 3652 FC).

Composition	86 wt% Tungsten carbide, 10 wt% Cobalt, 4 wt% Chromium
Size range used	+15 to -45 µm
Micro hardness	1000 to 1100 VHN
Density	14.61 g/cm^3

3.2.2 86WC10Co4Cr + 2 wt% yttrium oxide (Y_2O_3)

In this study, 2 wt% of yttrium oxide powder has been added to the existing 86WC10Co4Cr cermet. Yttrium oxide serves as another hard phase in addition to tungsten carbide, further improving the hardness and wear resistance of the coating. Yttrium oxide powder was procured from Alfa Aesar. Properties of the procured yttrium oxide are mentioned in Table 3.3. The two powders were mixed thoroughly in a jar mill for 12 hrs to produce the modified cermet.

Table 3.3: Properties of yttrium oxide.

Size used	10-15 µm
Morphology	Angular
Density	5.01 g/cm^3
Melting point	2425 °C

3.2.3 HVOF process and parameters

The HVOF coatings were done by Anod Plasma Spray Limited, Kanpur. JP-5000 liquid fuel HVOF system was used for the coatings. The gun was mounted on the arm of an automated 6-axis ABB robot which did the coating in several passes on the 13-4 MSS substrate. The process parameters of the HVOF process are shown in Table 3.4.

Table 3.4: HVOF process parameters.

Fuel	Kerosene
Kerosene flow rate	380-390 mL/min
Oxygen flow rate	850-900 slpm
Standoff distance	330 mm
Powder flow rate	70 g/min

Surface preparation for the HVOF process included grit blasting of the 13-4 MSS substrate to achieve a surface roughness (R_a value) of 6 µm. Increasing the surface roughness of the substrate is essential for getting strong mechanical interlocking between the coating and the surface. Average coating thickness achieved was around 350 µm. The two coatings and their nomenclature are shown in Table 3.5.

Table 3.5: Coating nomenclature.

Coating	Substrate	Substrate dimensions	Coating thickness	Nomenclature
86WC10Co4Cr	13-4 Martensitic Stainless Steel	20 mm × 20 mm × 6 mm	~ 350 µm	**WOKA**
86WC10Co4Cr + 2 wt% Y_2O_3	13-4 Martensitic Stainless Steel	20 mm × 20 mm × 6 mm	~ 350 µm	**WOKA + Y_2O_3**

The coated samples (WOKA and WOKA + Y_2O_3) are shown in Fig. 3.2.

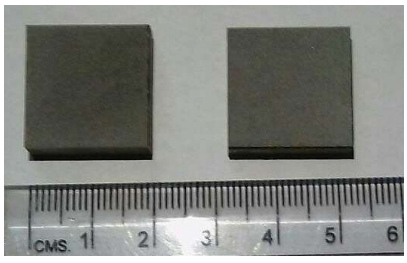

Figure 3.2: WOKA (left), WOKA + Y_2O_3 (right) coated samples.

3.3 Boronizing

Boronizing of 13-4 MSS was done using the pack boronizing method. It is a solid state process, hence, no melting takes place. A boronizing mixture was prepared consisting of 10 wt% boron carbide (B_4C - boron source), 5 wt% potassium tetrafluoroborate (KBF_4 - activator) and 85 wt% silicon carbide (SiC - inert material). Surface preparation included polishing the 13-4 MSS substrate (20 mm × 20 mm × 6 mm) on emery paper to 4/0 grit, followed by cleaning in acetone. The above mentioned boronizing mixture and 13-4 MSS substrate was then placed in a steel container such that the sample was completely buried in the mixture. The top of the container was covered with a steel lid and sealed with fire clay so that air cannot enter the container. The container was then placed in a muffle furnace at 900°C for 6 hrs. After the holding time, the sample was oil quenched and subsequently cleaned. Afterwards, another heat treatment was given to the sample by placing it in a muffle furnace at 500°C for 1 hr and then subsequently oil quenching it. This process led to an average coating thickness of 40 μm. Silicon carbide was procured from HIMEDIA in 220 mesh size. Boron carbide was procured from Lobachemie in 140 mesh size. Potassium tetrafluoroborate was procured from Sisco Research Laboratories Pvt. Ltd.

3.4 Coating characterization

Techniques used for characterization included SEM, EDS, XRD. Measurement of hardness and surface roughness were also taken.

3.4.1 SEM micrographs and Energy Dispersive Spectroscopy (EDS)

Microstructures of the samples were analyzed using Zeiss EVO 18 scanning electron microscope. Cross section of the coated samples (WOKA, WOKA + Y_2O_3 and boronized 13-4 MSS) were first polished to 4/0 emery paper followed by cloth polishing using a diamond paste. The polished samples were then mounted and SEM micrographs of the cross section were taken. The coating thickness was measured. SEM micrographs of the surface of all samples were also taken before and after the wear test. Energy Dispersive Spectroscopy (EDS) analysis of the samples was also done to determine the elements present in the coatings.

3.4.2 X-ray diffraction (XRD) analysis

To find out the phases present in the coatings, XRD analysis was carried out using Rigaku SmartLab X-Ray diffractometer with cobalt target. PANalytical X'pert High Score Plus was used for matching the diffraction pattern with the reference PDF 2-2016.

3.4.3 Micro hardness

Micro hardness of 13-4 MSS and coated samples (WOKA, WOKA + Y_2O_3 and boronized 13-4 MSS) was taken using a Vickers hardness testing machine at a load of 25 g and holding time of 10 sec.

3.4.4 Surface roughness

Surface roughness of 13-4 MSS and coated samples before and after the wear test was determined by a Mitutoyo Surface Profilometer.

3.5 Slurry pot wear testing

A custom built slurry pot wear testing machine was used to investigate the wear resistance of 13-4 MSS and the two coated samples. The machine was built by modifying an existing drilling machine (Fig. 3.3). The motor was replaced by a variable speed frequency driven motor and a control box. The tool head was replaced by a holder in which the samples were secured. A bucket with baffles built into it was kept on the workbench just under the holder. The slurry was prepared in the bucket. The holder was then lowered into the bucket such that the samples were completely submerged in the slurry. The motor was then turned on and its frequency was varied to get the required speed. The holder was built in such a way that only the coated surface of the sample was exposed to the abrasive slurry.

The MSS sample was polished to 1500 cw emery paper while WOKA and WOKA + Y_2O_3 coated samples were not polished. Samples were then weighed on a Mettler electronic balance having a least count of 0.1 mg. Samples were then secured in the holder and lowered into the slurry. The process parameters of the slurry test are mentioned in Table 3.6. The test ran for a total of 40 hrs with observations taken after every 8 hrs to determine the weight loss. The

cumulative weight loss was then converted into volumetric wear loss and further divided by the area of the exposed surface to give volumetric wear loss per unit area. A graph was then plotted between volumetric wear loss per unit area and time for each of the samples.

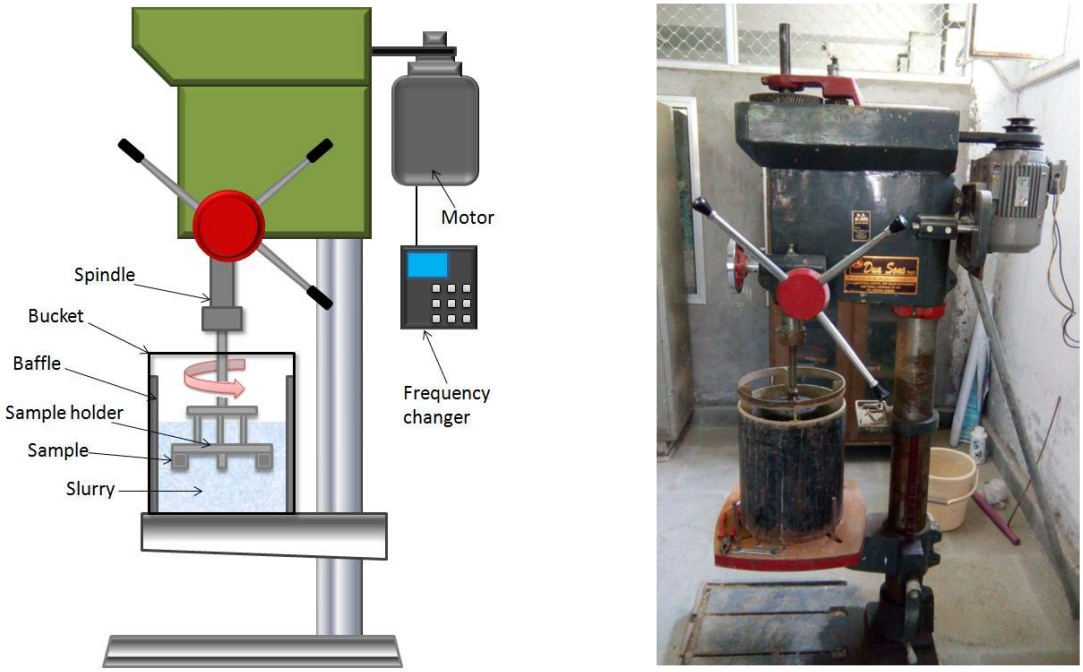

(a) (b)

Figure 3.3: (a) Schematic diagram of slurry pot tester (b) Slurry pot tester actually used.

Table 3.6: Slurry pot erosion process parameters.

Erodent used	Silica sand
Size range	210 µm to 297 µm
Concentration	100 g/L
Rotational speed	500 RPM
Center to sample distance	9 cm
Sliding velocity	4.45 m/s
Total testing time	40 hrs
Observations taken after	Every 8 hrs

Chapter 4

Results and Discussion

Erodent particle, coating powders, 13-4 MSS substrate, HVOF coatings, boronized 13-4 MSS samples were characterized using SEM, EDS and XRD. Further, hardness and surface roughness of the coatings were also determined. A wear curve between cumulative volumetric wear and time was also plotted for all the samples. The results have been summarized below -

4.1 SEM micrographs

SEM micrographs of erodent particle, coating powders, substrate and coating surfaces were taken using Zeiss EVO 18 scanning electron microscope.

4.1.1 Erodent particle (silica sand)

Figure 4.1 shows the SEM micrograph of the erodent particles, silica sand. The particles have an angular morphology with an average size range between 200 and 300 μm. This sand was used for the slurry pot testing.

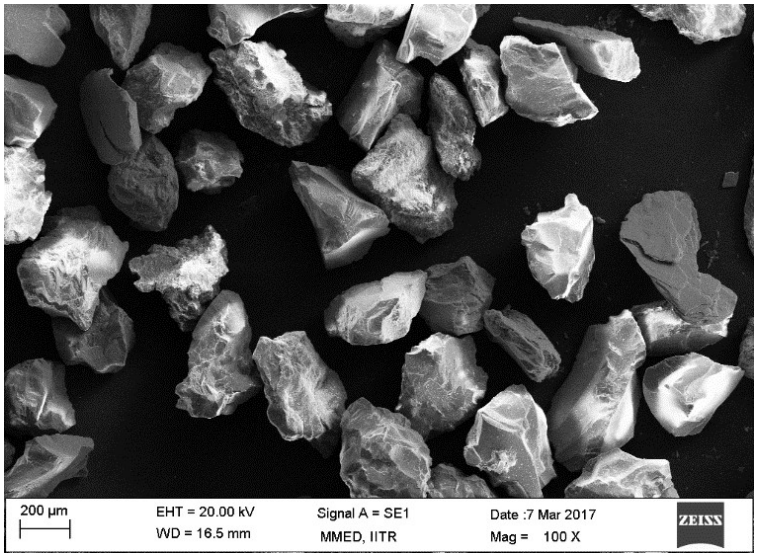

Figure 4.1: SEM micrographs of the erodent particles silica sand.

4.1.2 Y_2O_3 powder

Figure 4.2 shows the SEM micrographs of Y_2O_3 powder used. The powder is of angular morphology with size range of approximately 10 μm.

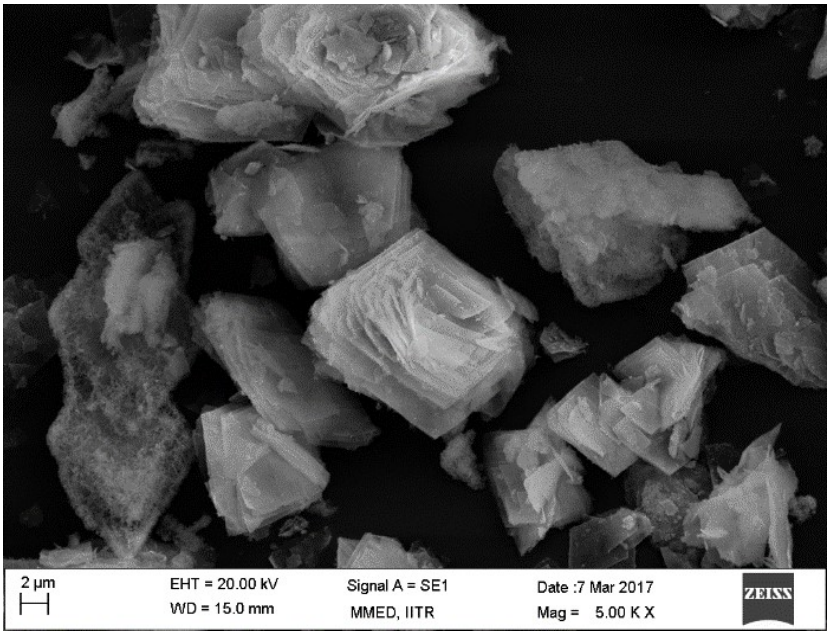

(a)

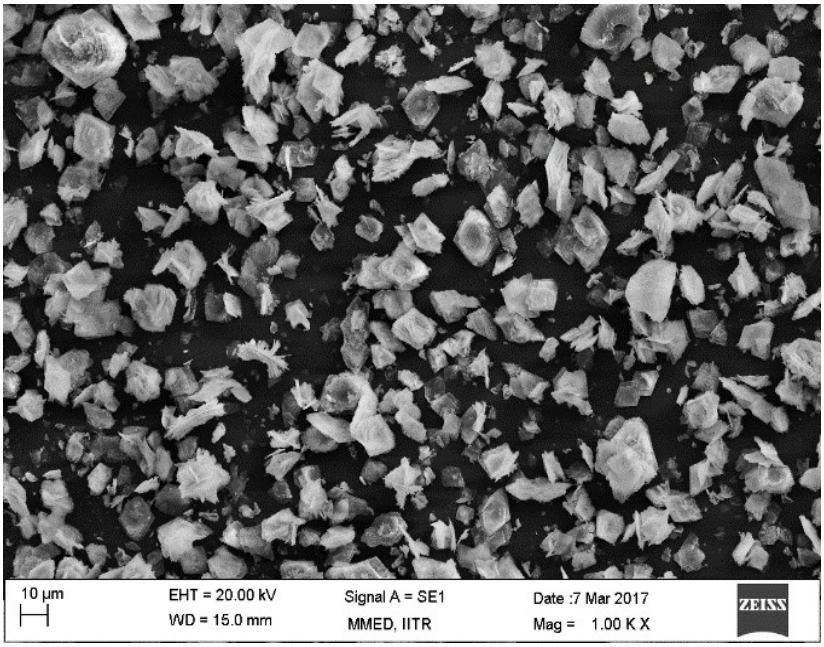

(b)

Figure 4.2: SEM micrographs of Y_2O_3 powder used (a) 5000x (b) 1000x.

4.1.3 WOKA + Y_2O_3 powder

Figure 4.3 shows the SEM micrograph of the modified cermet (WOKA + Y_2O_3). WOKA particles are big and spherical with a size range between 15 and 45 µm. While the Y_2O_3 particles are small and angular with a size range of approximately 10 µm. Y_2O_3 particles seem to be evenly distributed with the WOKA particles.

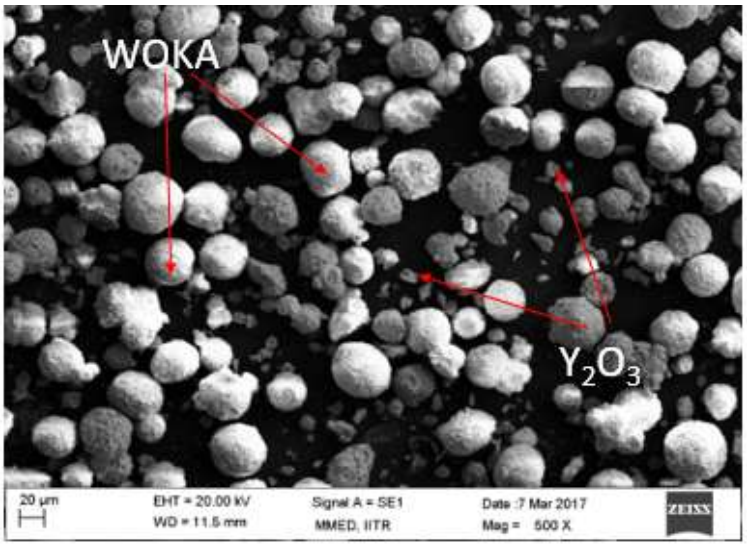

Figure 4.3: SEM micrograph of the modified cermet WOKA + Y_2O_3.

4.1.4 13-4 MSS substrate

Figure 4.4 shows the SEM micrograph of 13-4 MSS substrate used for the coatings before wear. The directional scratches are from polishing on emery papers.

4.1.5 HVOF coatings

Figure 4.5 shows the SEM micrograph of the cross-section of WOKA and WOKA + Y_2O_3. The cross section of the samples shows a dark coloured substrate (13-4 MSS) and a light coloured coating (Cermet) on top of it. The average coating thickness achieved for WOKA and WOKA + Y_2O_3 is about 350 µm.

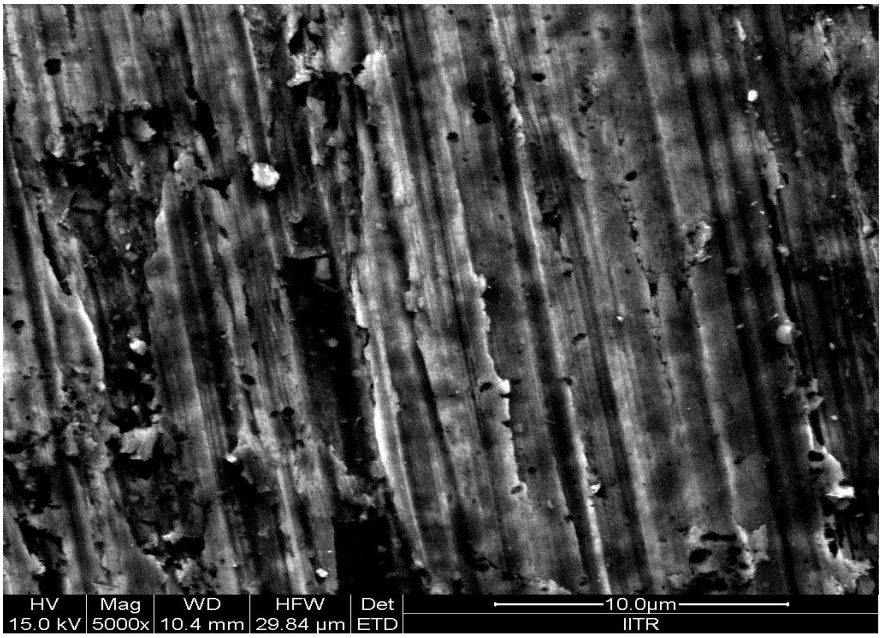

Figure 4.4: SEM micrograph of 13-4 MSS substrate.

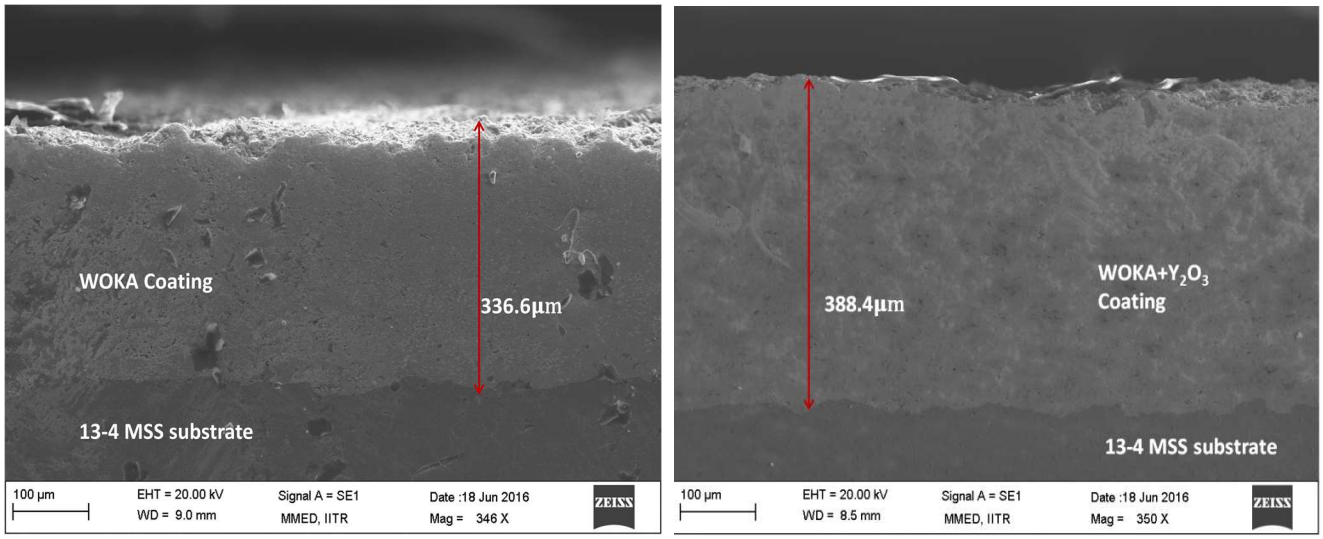

(a) (b)

Figure 4.5: SEM micrographs of the cross section of (a) WOKA (b) WOKA + Y_2O_3.

Figure 4.6 shows the SEM micrograph of the surface of WOKA and WOKA + Y_2O_3 before wear. The splat structure can be easily identified in the coated samples which is characteristic of HVOF coatings.

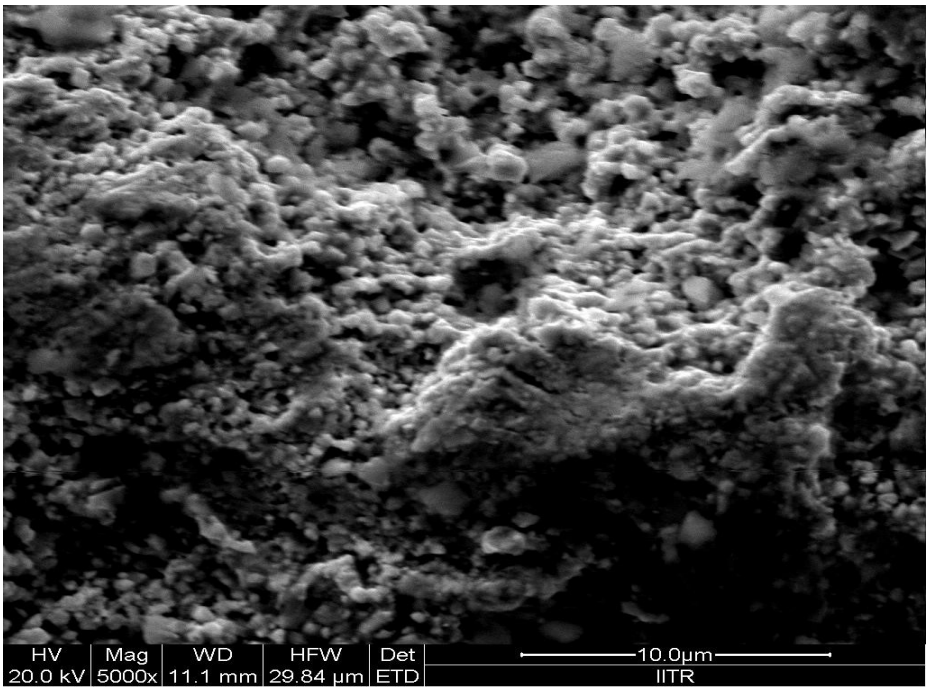

(a)

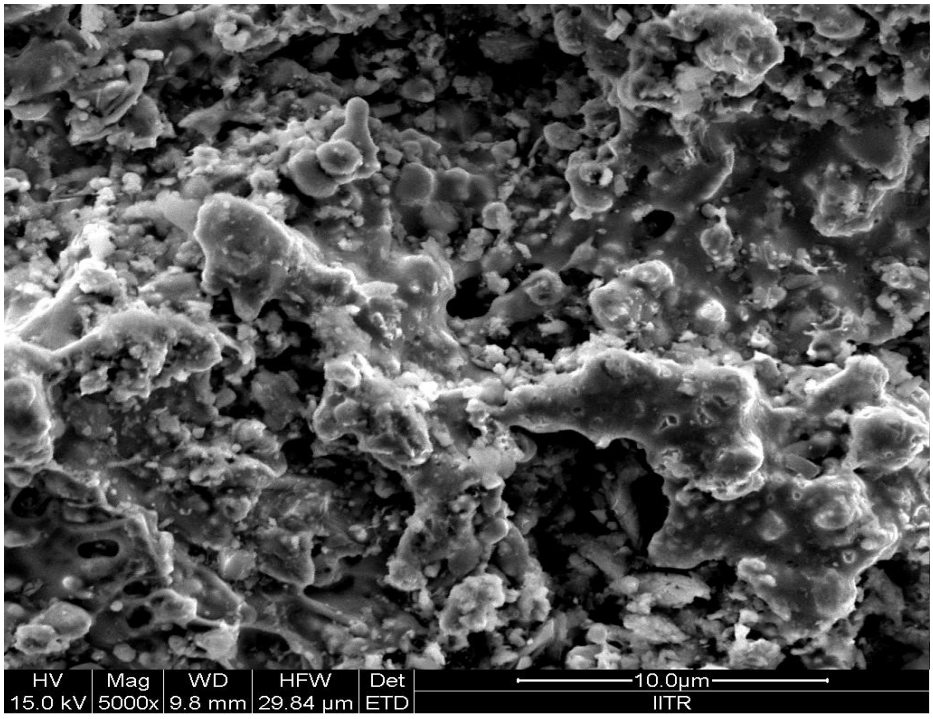

(b)

Figure 4.6: SEM micrographs of the top surfaces of (a) WOKA (b) WOKA + Y_2O_3 before wear.

4.1.6 Boronizing

Figure 4.7 (a) shows the cross section of the boronized 13-4 MSS sample. A boride layer of average thickness 40 µm can be seen. The boride layer formed on 13-4 MSS substrate is quite smooth and continuous as compared to the finger shaped boride layers usually formed on the low alloy steels. This is due to the high percentage of chromium (13.35 wt%) in 13-4 MSS which slows the diffusion process resulting in a smoother interface between the boride layer and substrate [Kayali et al., 2013].

The boronized 13-4 MSS samples show three distinct regions (Fig. 4.7 (b)). The outermost layer is the smooth boride layer consisting of FeB and Fe_2B phases. Below this layer, there is a solid solution of boron in the transition zone. Below this layer is the unaffected 13-4 MSS substrate.

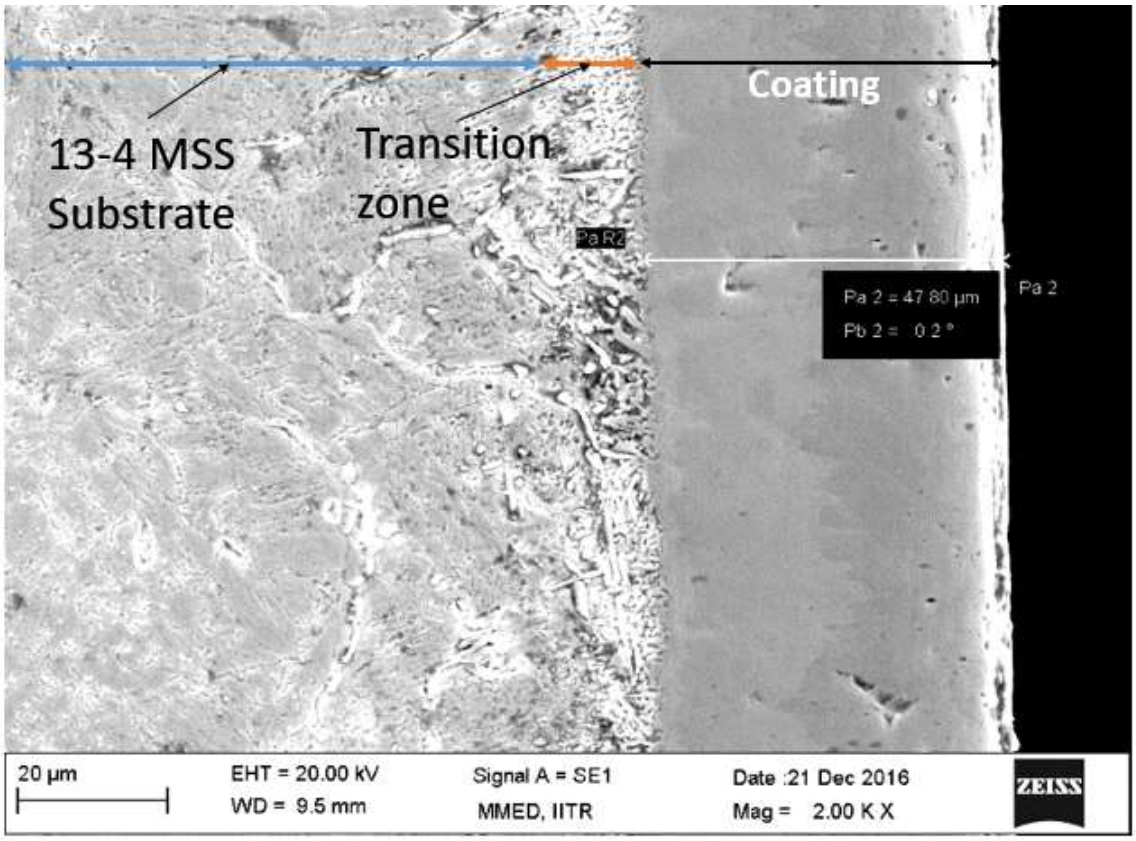

(a)

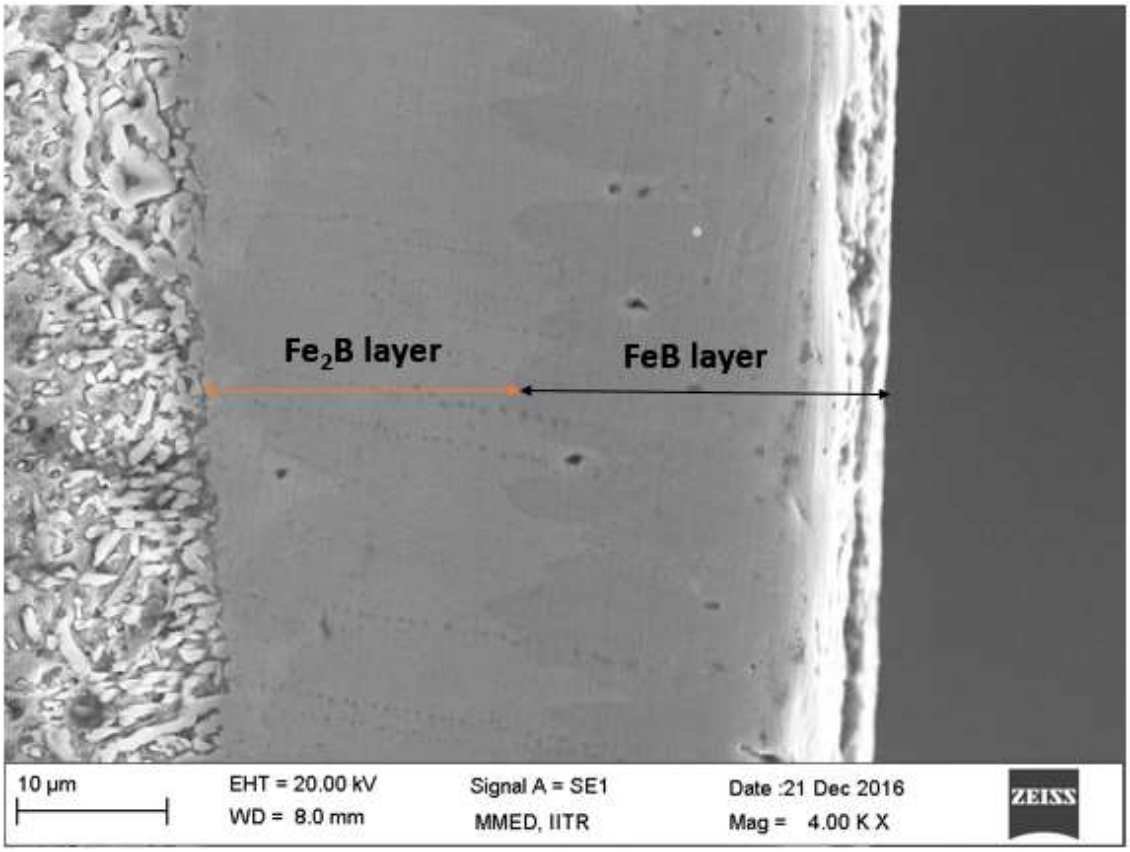

(b)

Figure 4.7: Cross section of the boronized 13-4 MSS sample at (a) 2000x (b) 4000x.

4.2 EDS analysis

EDS analysis of the coating powders and coating surface was done using Zeiss EVO 18 scanning electron microscope.

4.2.1 Y_2O_3 powder

EDS analysis of the Y_2O_3 powder confirmed the presence of the elements yttrium and oxygen. The composition by weight is shown in Fig. 4.8.

4.2.2 WOKA + Y_2O_3 powder

EDS analysis of the modified cermet powder WOKA + Y_2O_3 confirmed the presence of the elements tungsten, cobalt, chromium and carbon in the spherical WOKA particle and the

presence of elements yttrium and oxygen in the angular Y_2O_3 particle. The composition by weight is shown in Fig. 4.9.

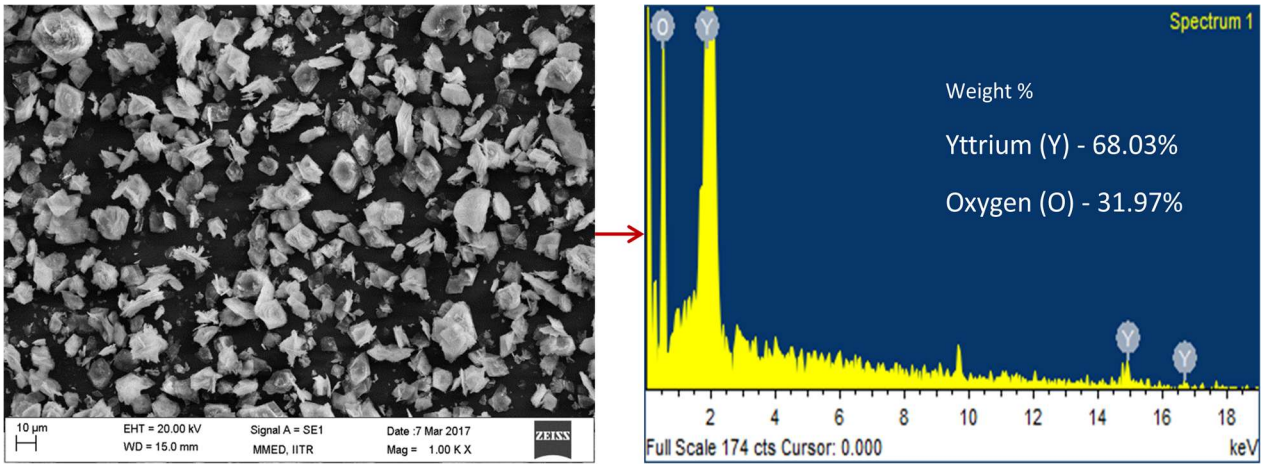

Figure 4.8: SEM micrograph of Y_2O_3 particles with EDS analysis.

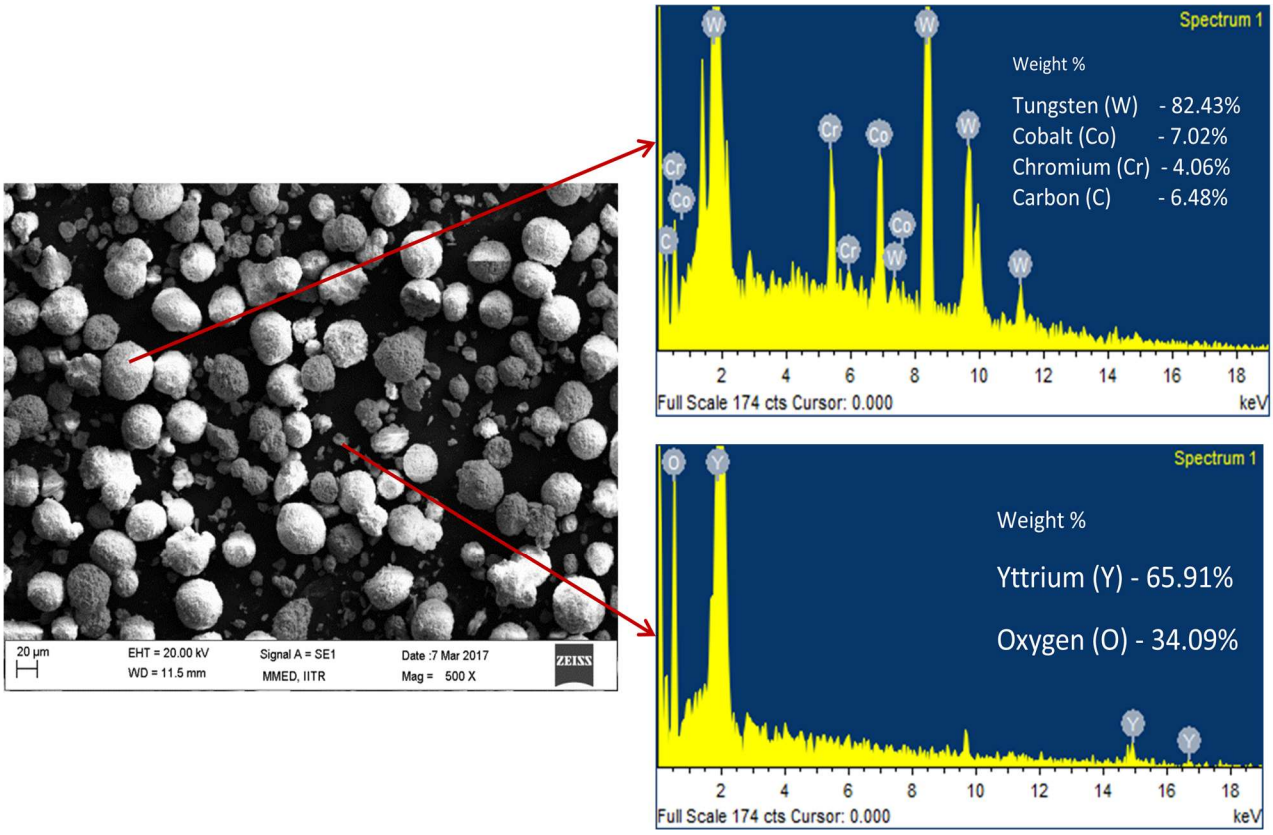

Figure 4.9: SEM micrograph of WOKA + Y_2O_3 powder with EDS analysis.

4.2.3 WOKA coatings

EDS analysis of the cermet coating WOKA confirmed the presence of the elements tungsten, cobalt, chromium and carbon. Also, EDS analysis of the cermet coating WOKA + Y_2O_3 confirmed the presence of the elements– tungsten, cobalt, chromium, carbon and yttrium. The composition by weight of the two coatings is shown in Fig. 4.10.

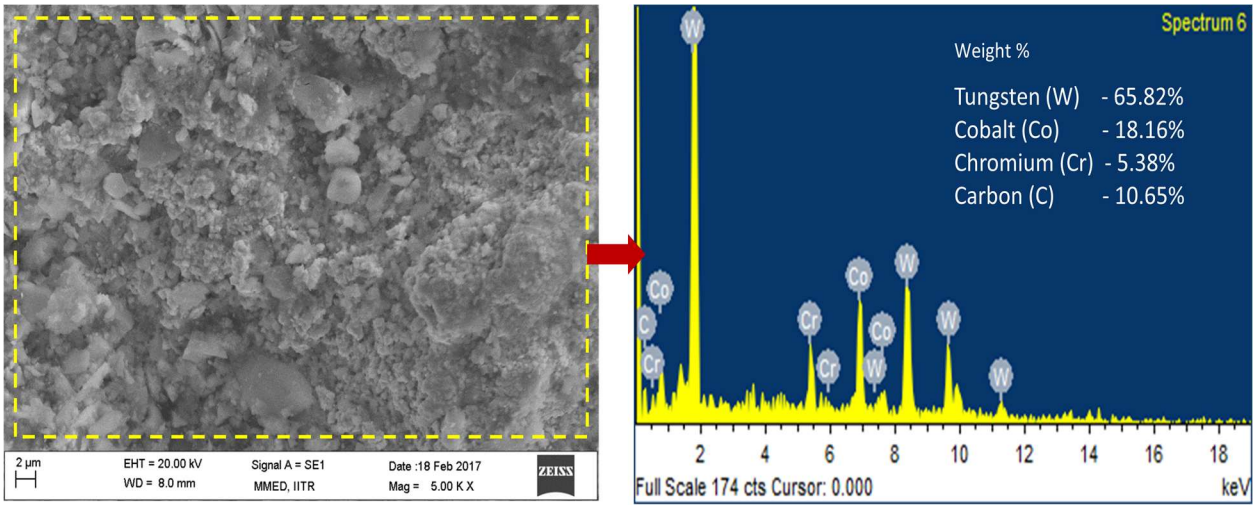

(a)

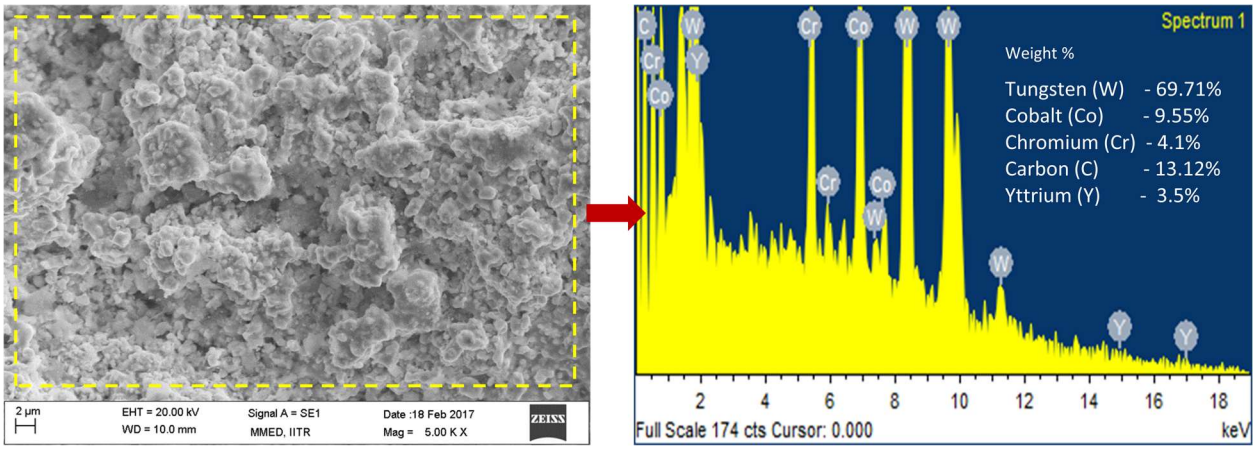

(b)

Figure 4.10: SEM micrographs of the surfaces of (a) WOKA (b) WOKA + Y_2O_3 before wear with EDS analysis.

4.3 XRD analysis

Figure 4.11 depicts the XRD pattern of WOKA coating. WC was found to be the major phase present in the sample with Co_6W_6C phase also present due to decarburization of WC particles. The diffraction peak pattern with 2θ values 31.707°, 35.892°, 48.652°, 64.678°, 73.330°, 76.084°, 99.49° and 108.357° correspond to (0 0 1), (1 0 0), (1 0 1), (0 0 2), (1 1 1), (1 0 2), (1 1 2) and (0 0 3) crystal planes of WC respectively, matching with reference PDF-2 2016. Similarly, the diffraction peak pattern with 2θ values 35.892°, 40.453°, 43.081°, 47.124° and 73.595° correspond to (3 3 1), (4 2 2), (5 1 1), (4 4 0) and (6 6 0) crystal planes of Co_6W_6C respectively, matching with reference PDF-2 2016.

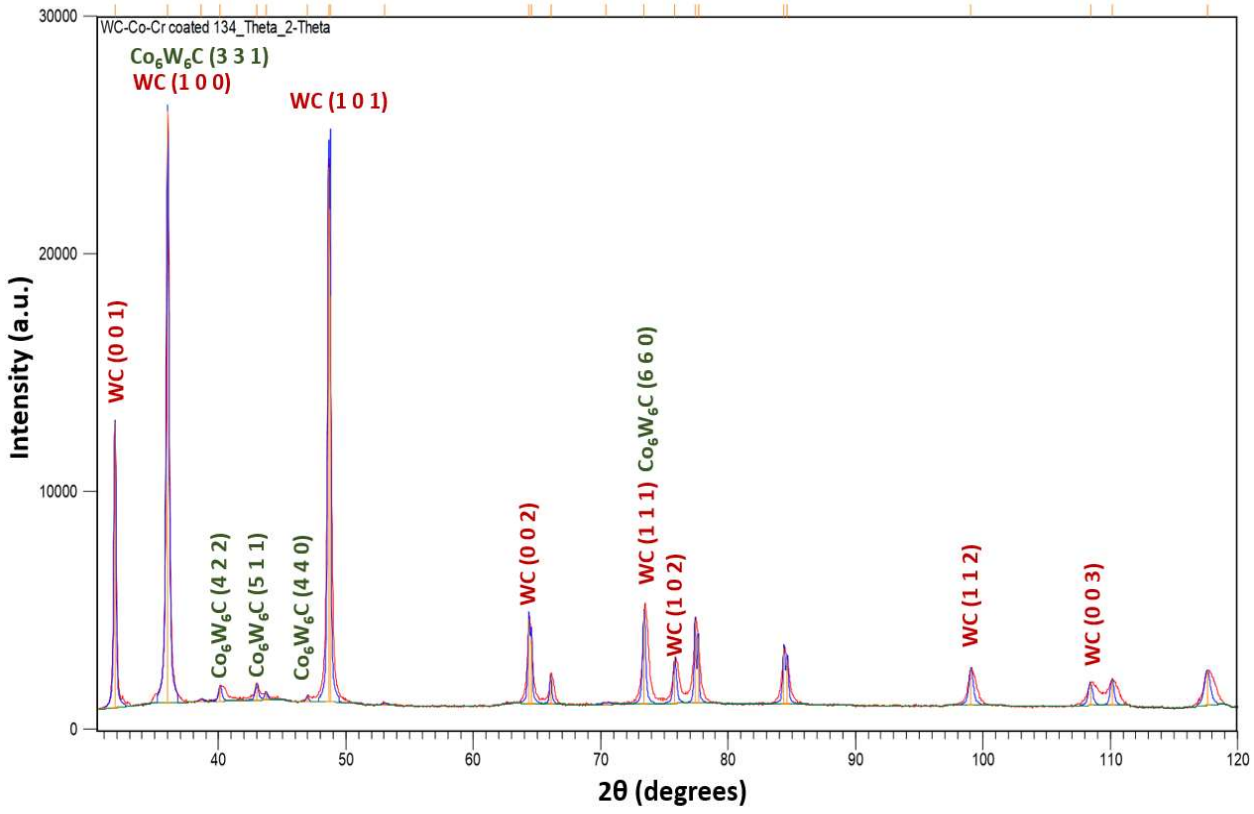

Figure 4.11: XRD pattern of WOKA coating.

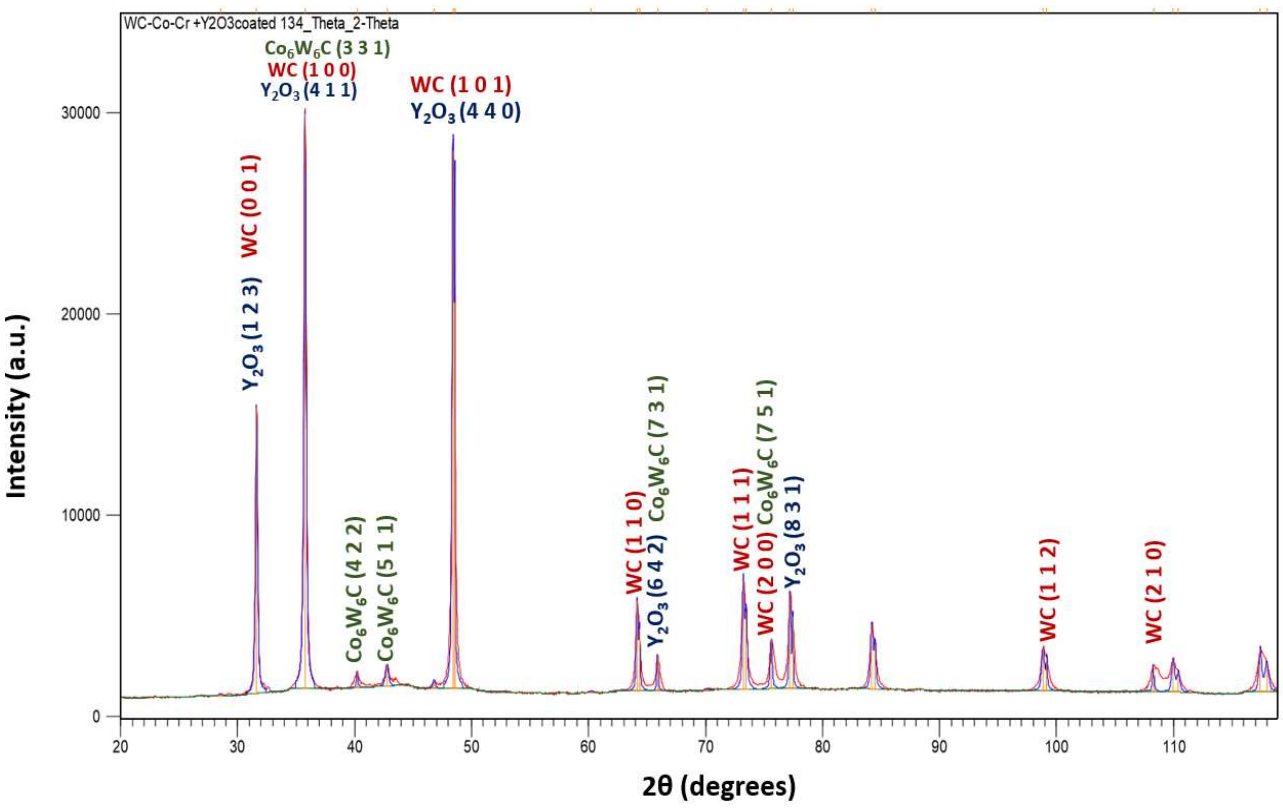

Figure 4.12: XRD pattern of WOKA + Y_2O_3 coating.

Figure 4.12 depicts the XRD pattern of WOKA + Y_2O_3 coating. WC was found to be the major phase present in the sample with Co_6W_6C phase also present due to decarburization of WC particles. Y_2O_3 was also found to be present in the pattern. Diffraction peak pattern with 2θ values 31.475°, 35.598°, 48.376°, 64.179°, 73.330°, 75.374°, 99.49° and 108.357° correspond to (0 0 1), (1 0 0), (1 0 1), (1 1 0), (1 1 1), (2 0 0), (1 1 2) and (2 1 0) crystal planes of WC respectively, matching with reference PDF-2 2016. Similarly, the diffraction peak pattern with 2θ values 36.041°, 40.606°, 43.167°, 65.860° and 75.656° correspond to (3 3 1), (4 2 2), (5 1 1), (7 3 1) and (7 5 1) crystal planes of Co_6W_6C respectively, matching with reference PDF-2 2016. Also, the diffraction peak pattern with 2θ values 31.533°, 35.890°, 48.510°, 65.836° and 77.320° correspond to (1 2 3), (4 1 1), (4 4 0), (6 4 2) and (8 3 1) crystal planes of Y_2O_3 respectively, matching with reference PDF-2 2016.

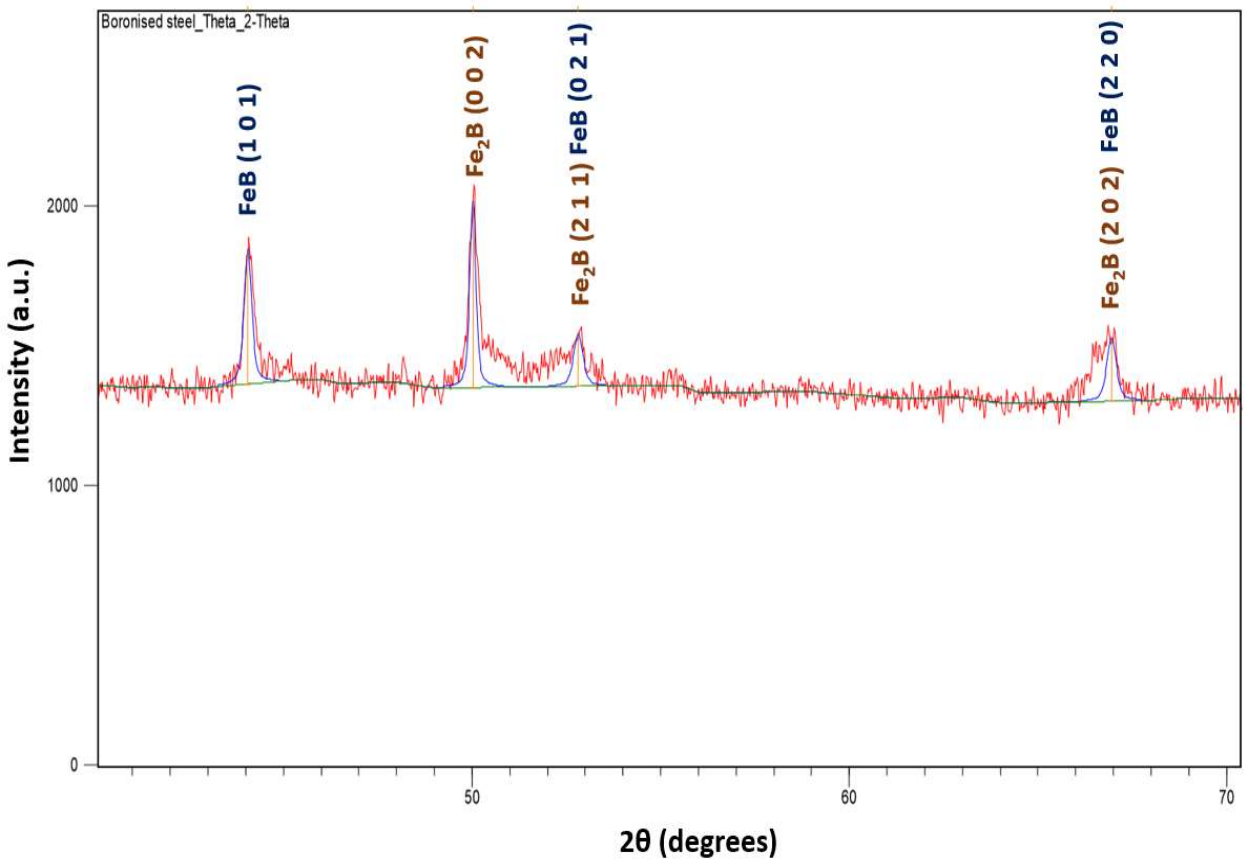

Figure 4.13: XRD pattern of boronized 13-4 MSS sample.

Figure 4.13 depicts the XRD pattern of boronized 13-4 MSS sample. FeB and Fe_2B are found to be the two major phases present in the sample. Diffraction peak pattern with 2θ values 49.914°, 52.850° and 66.566° correspond to (0 0 2), (2 1 1) and (2 0 2) crystal planes of Fe_2B respectively, matching with reference PDF-2 2016. Also, the diffraction peak pattern with 2θ values 44.075°, 52.805° and 66.405° correspond to (1 0 1), (0 2 1) and (2 2 0) crystal planes of FeB respectively, matching with reference PDF-2 2016.

4.4 Surface roughness

Table 4.1 shows the surface roughness (R_a) values before and after the wear test. Surface roughness values were taken using a contact type Mitutoyo surface profilometer.

Table 4.1: Surface roughness (R_a) values before and after the wear test.

Sample	R_a value before wear (μm)	R_a value after wear (μm)
13-4 MSS	0.1	0.08
WOKA	4.84	4.7
WOKA + Y_2O_3	4.96	4.51

4.5 Micro hardness

Table 4.2 shows the micro hardness (VHN) of 13-4 MSS, WOKA, WOKA + Y_2O_3 and boronized 13-4 MSS at 25 g loading. Also, boronized 13-4 MSS has the highest value of micro hardness as compared to the other samples.

Table 4.2: Micro hardness (VHN) values of MSS, WOKA and WOKA + Y_2O_3 at 25g loading.

Sample	Micro hardness (VHN)
13-4 MSS	302
WOKA	1050
WOKA + Y_2O_3	1150
BORONIZED 13-4 MSS	1655

4.6 Wear curve

A wear curve is drawn between the cumulative volumetric wear per unit area and time for all the samples as shown in Fig. 4.14. During the initial run in period of about 8 hrs, there is not much significant difference in wear rates between the two HVOF coatings (WOKA, WOKA + Y_2O_3) and 13-4 MSS. WOKA and WOKA + Y_2O_3 have larger surface roughness (R_a) values before wear than 13-4 MSS (Table 4.1). This explains the higher wear for the HVOF coated samples during the initial run in period as higher surface roughness leads to higher wear. After the 8 hrs period, the HVOF coated samples start to perform better than 13-4 MSS as is evident from the lower values of cumulative volumetric wear. Also, the wear rate (slope) for the HVOF coated samples decreases drastically after the initial run in period, while that for the 13-4 MSS does not decrease by a significant amount. Clearly, WOKA and WOKA + Y_2O_3 have much higher values of hardness (Table 4.2) (1050 and 1150 VHN, respectively) than the 13-4 MSS (302 VHN). This

explains the lower wear for the HVOF coated samples after the run in period as compared to the 13-4 MSS. Higher hardness leads to erosion resistance.

The wear curve of WOKA + Y_2O_3 lies under the curve of WOKA for all the duration. This suggests that WOKA + Y_2O_3 has better wear resistance than WOKA. Hence, the addition of Y_2O_3 in the WOKA cermet led to some improvement in the wear resistance. This can be explained on the basis of the higher hardness of WOKA + Y_2O_3 (1150 VHN) than WOKA (1050 VHN) coating (Table 4.2). A 25% reduction in volumetric wear is observed in WOKA + Y_2O_3 as compared to the 13-4 MSS and 11% reduction is observed as compared to the WOKA coating. Although, the improvement in the wear performance is not as much as expected due to the increased porosity of the WOKA + Y_2O_3 coating.

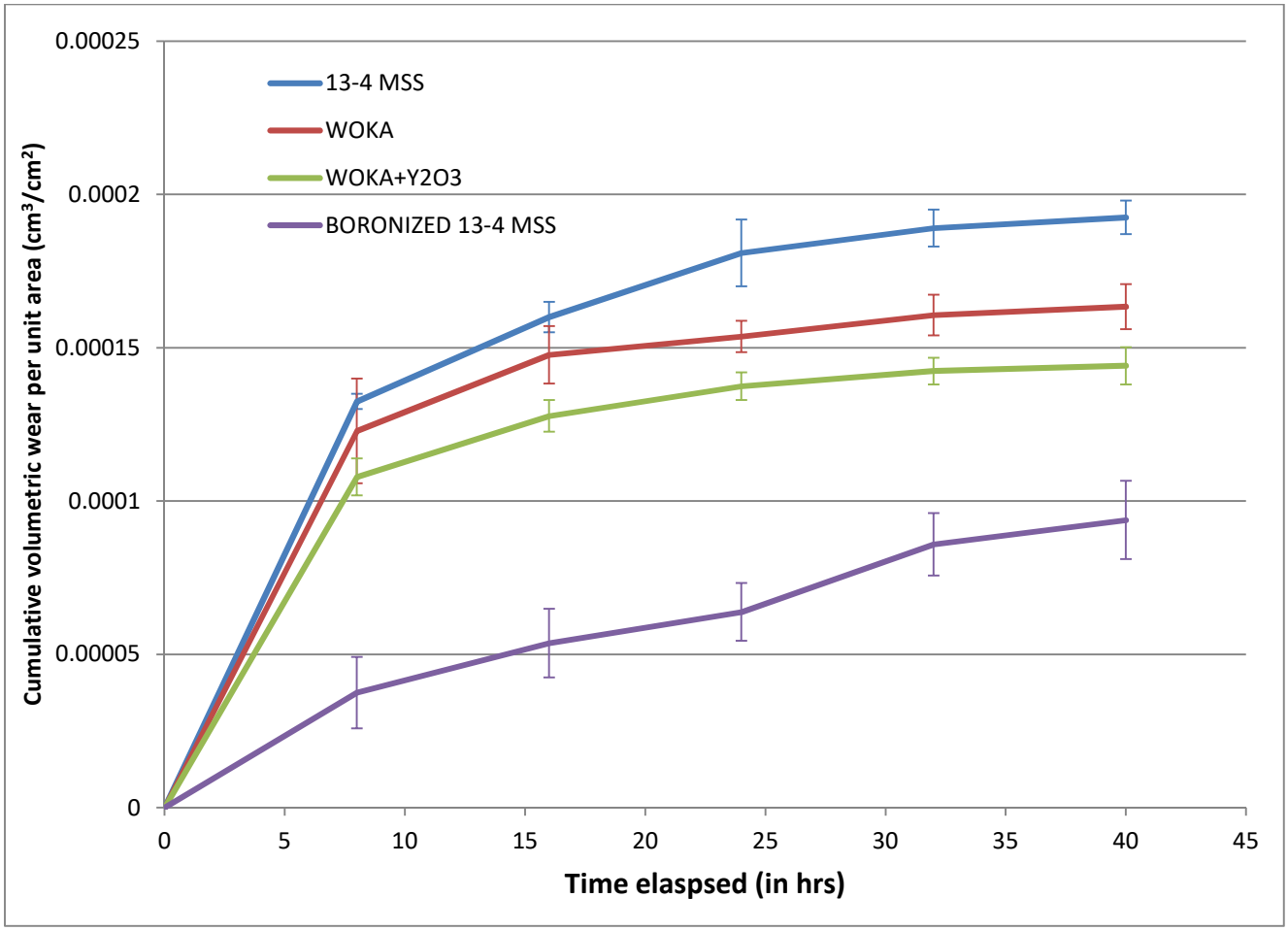

Figure 4.14: Wear curve between cumulative volumetric wear per unit area and time for all samples.

The boronized 13-4 MSS sample exhibited superior wear resistance than the 13-4 MSS and even the HVOF coated samples during the 8 hrs run in period and after it. This is attributed to the exceptionally higher hardness of boronized 13-4 MSS (1655 VHN). Approximately 50% reduction in volumetric wear is observed in the boronized 13-4 MSS as compared to the bare 13-4 MSS.

4.7 SEM micrographs after wear

Figure 4.15 shows the SEM micrograph surface of 13-4 MSS sample after the wear test. On observation, the surface of the eroded sample appears smoother than the original 13-4 MSS sample (Fig. 4.4). This is also supported by the decrease in the surface roughness values from 0.1 to 0.08 μm after the wear test (Table 4.1). The main mechanism of material removal for ductile materials is by repeated deformation and micro cutting [Hutchings, 1992]. The eroded surface shows the presence of micro cutting and micro ploughing along with craters and lips that are formed as a result of it (Fig. 4.15 (b)). These observations are in accordance with the ductile mode of erosion.

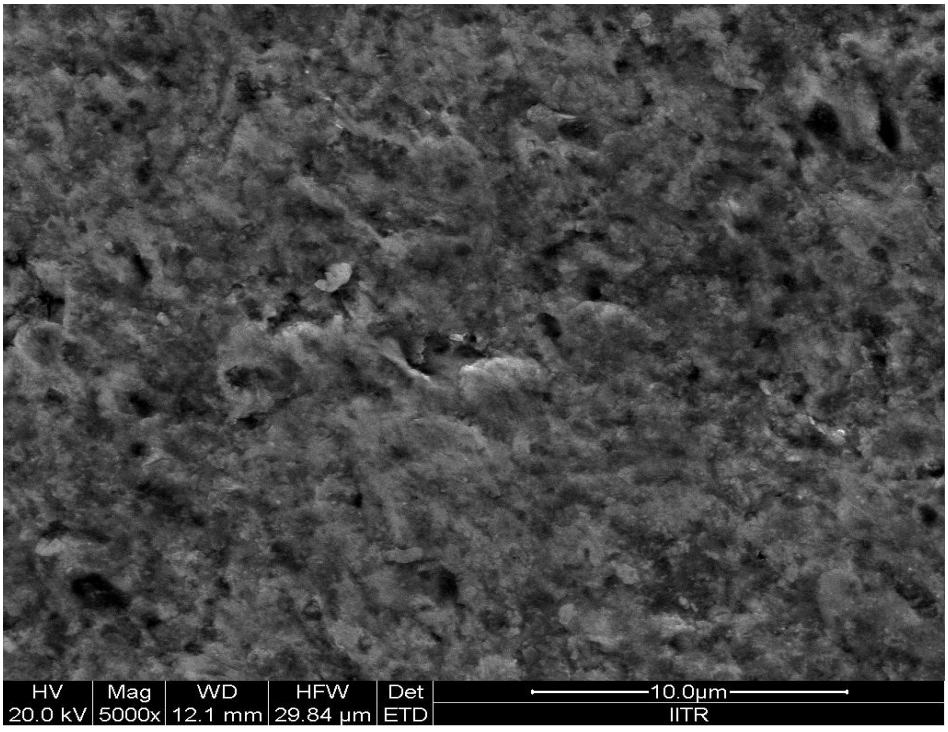

(a)

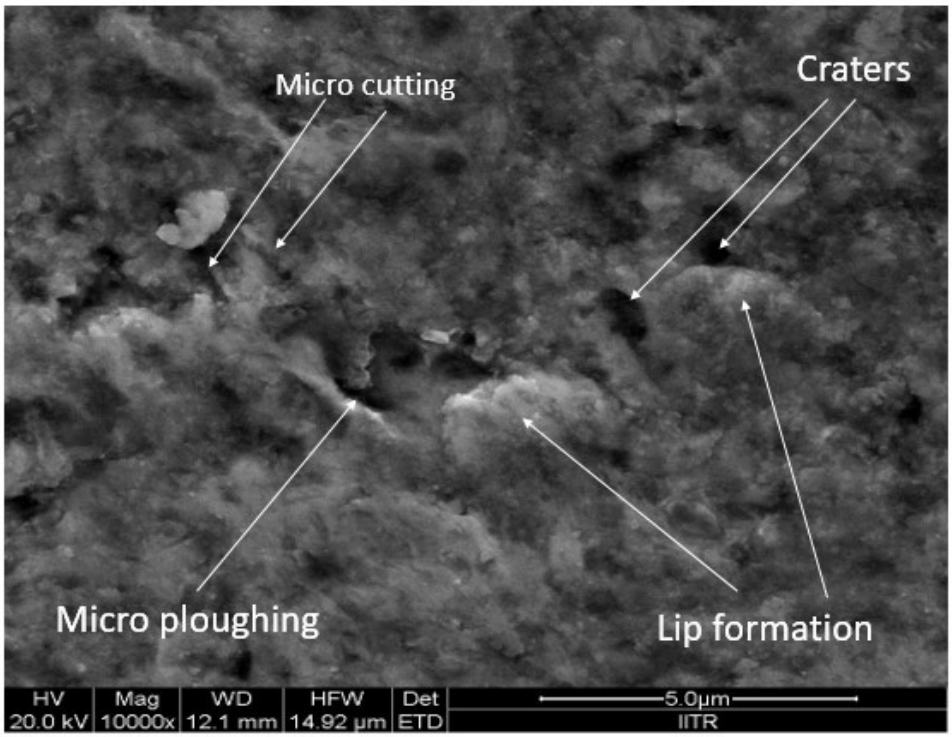

(b)

Figure 4.15: SEM micrograph surface of 13-4 MSS sample after wear test at (a) 5000x (b) 10000x.

Figure 4.16 shows the SEM micrograph of the surface of WOKA coating after wear test. The eroded surface of the coatings appears smoother than the original coating (Fig. 4.6 (a)). This observation is also supported by the reduction in surface roughness value from 4.84 to 4.70 µm after the wear test (Table 4.1). The main mechanism of material removal seems to be the removal of the metal matrix/binder by micro cutting followed by the subsequent pulling out of the tungsten carbide grains [Goyal et al., 2012] (Fig. 4.16 (a)). Some micro cutting and detachment of unmelt particles can also be seen in Fig. 4.16 (b). Hence, the mode of erosion is mainly ductile.

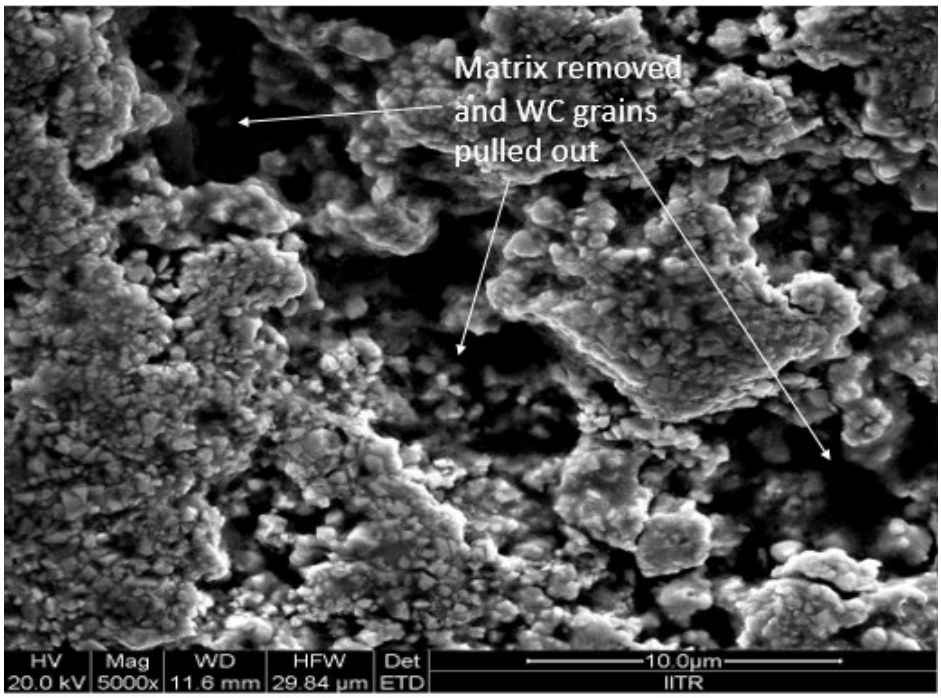

(a)

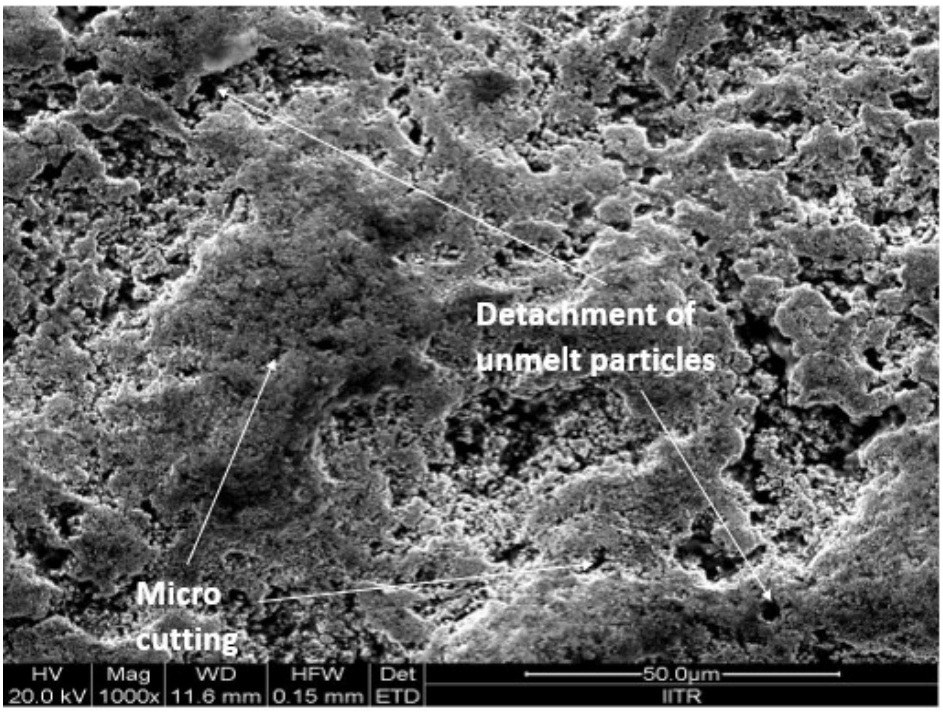

(b)

Figure 4.16: SEM micrograph of the surface of WOKA coating after wear test at (a) 5000x (b) 1000x.

Figure 4.17 shows the SEM micrograph of the surface of WOKA + Y_2O_3 coating after wear test. The eroded surface of the coatings appears smoother than the original coating (Fig. 4.6 (b)). This observation is also supported by the reduction in surface roughness from 4.96 to 4.51 µm value after the wear test (Table. 4.1). The mode of erosion is same as that of the WOKA coating i.e. micro cutting of the binder matrix followed by pull out of the WC grains. Although, the extent of erosion is observed to be less in WOKA + Y_2O_3 than in WOKA on account of its better wear resistance (Fig. 4.14).

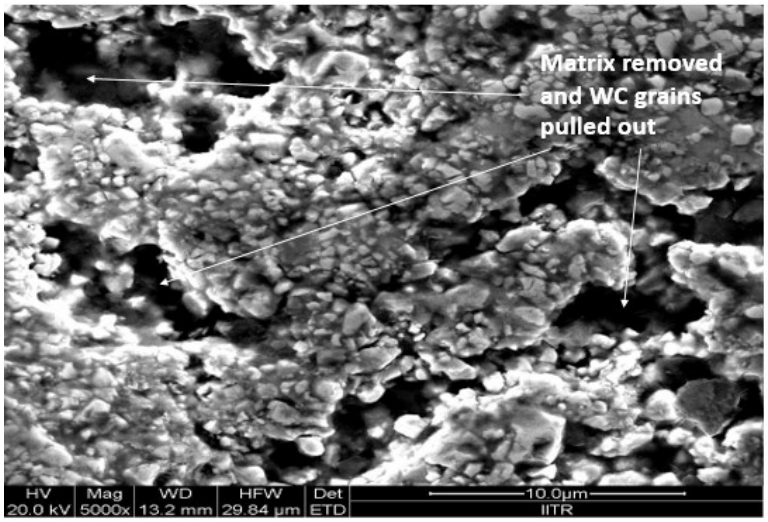

(a)

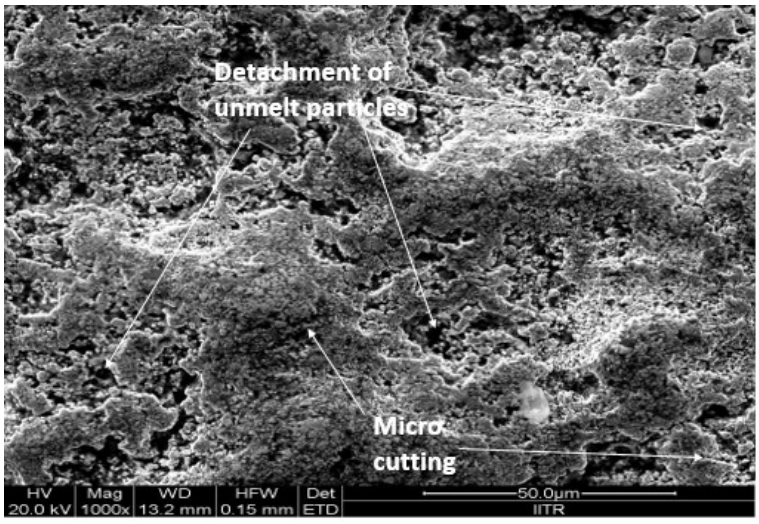

(b)

Figure 4.17: SEM micrograph of the surface of WOKA + Y_2O_3 coating after wear test at (a) 5000x (b) 1000x.

Figure 4.18 shows the SEM micrograph of boronized 13-4 MSS surface after wear. The surface of the sample shows the presence of a number of pits. Since, the outermost FeB layer is very hard, the main mechanism of wear was found to be brittle fracture - silt particles repeatedly striking a particular area on the surface till it cracks and chips off. The amount of material removed during wear was so small that polishing marks from before wear are still visible. This is also supported by the superior wear resistance of the boronized 13-4 MSS (Fig. 4.14).

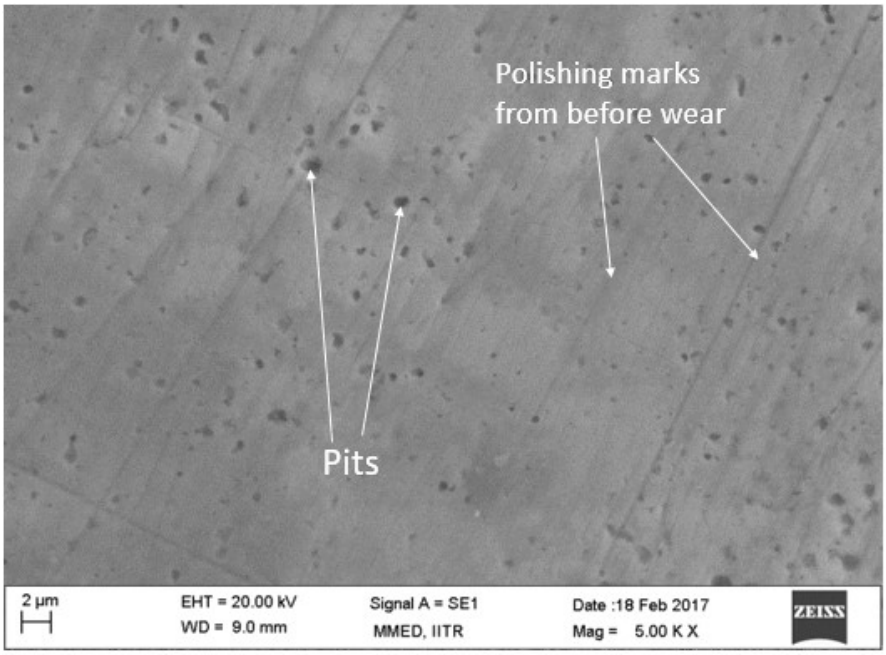

Figure 4.18: SEM micrograph of boronized 13-4 MSS surface after wear.

Chapter 5

Discrete Phase Modelling

ANSYS FLUENT was used for the CFD modelling of the silt erosion phenomenon. Discrete phase modelling (DPM) was used for the treatment of the silt particles while k-ε model was used for the liquid phase. Two geometries were selected for the simulation –

- Pelton turbine nozzle and spear arrangement
- Pelton turbine runner

The steps in the modelling process were -

1. First, a geometry was chosen for the modelling. The geometries used were based off of real world hydro turbine components with identical dimensions and operational parameters.
2. The geometry was then constructed in a CAD modeler like Solidworks.
3. The geometry was then imported into ANSYS FLUENT.
4. A mesh was then generated on the geometry. Mesh generation was done keeping in mind good quality and resolution.
5. A model was then chosen for the continuous (liquid) flow - k-ε model.
6. For the silt particles, the discrete phase model (DPM) was chosen.
7. DPM injections were set up along with the properties of the material to be injected.
8. Cell zone and boundary conditions for the problem were set up.
9. While the geometry was stationary for the Pelton nozzle and spear, rotary motion was given to the rotor of the Pelton turbine runner.
10. For the steady state simulation in Pelton nozzle and spear, number of iterations was assigned for the calculations. While for the unsteady simulation in Pelton runner, number of time steps and step size were assigned.
11. The problem was then initialized and run till the solution converged.
12. The results were then analyzed in post processing.

5.1 Formulation of the problem

For modelling silt erosion phenomenon, two geometries from Pelton turbine have been used.

5.1.1 Pelton turbine nozzle and spear (partially open condition)

Pelton turbine nozzle and spear arrangement is quite susceptible to erosion by silt particles, hence, it was chosen for the study. The dimensions and operating conditions have been taken from the work of Benzon et al. [2015] on impulse turbine (Table.5.1).

Table 5.1: Dimensions and operating conditions for the Pelton turbine nozzle and spear [Benzon et al., 2015].

Inlet Manifold Diameter **8.18 cm**	Nozzle Diameter **3.10 cm**
Spear angle **50°**	Nozzle angle **90°**
Inlet fluid pressure **1 MPa (Gauge)**	Inlet fluid velocity **4.4 m/s**
Silt particle dia. **250 µm**	Silt concentration **0.0005 kg/s (20 ppm)**
Spear Material **Carbon steel**	Steady State Problem

Three cases were studied-

- **Location of erosion on spear studied.**
  Silt particle size 250 µm, silt mass flow rate 0.0005 kg/s, inlet fluid velocity 4.4 m/s, inlet fluid pressure 1 MPa.
- **Silt mass flow rate varied and effect on erosion rate studied.**
  Silt mass flow rate used are 0.0001, 0.0003 and 0.0005 kg/s, silt particle size 250 µm, inlet fluid velocity 4.4 m/s and inlet fluid pressure 1 MPa.
- **Fluid inlet velocity varied and effect on erosion rate studied.**
  Fluid inlet velocity used are 4, 4.5 and 5 m/s, silt particle size 250 µm, silt mass flow rate 0.0005 kg/s, inlet fluid pressure 1 MPa.

5.1.2 Pelton turbine runner

The dimensions and operating conditions of the runner were calculated using correlations suggested by Dr. P. M. V. Subbarao (Professor, Mechanical Engineering Department, IIT Delhi) based on the jet diameter (Table 5.2).

Table 5.2: Dimensions and operating conditions for the Pelton turbine runner.

Runner diameter **1.7 m**	Outer radius of the runner **103 cm**
Inner radius of the runner **67 cm**	Speed **300 RPM**
No. of buckets **22**	No. of buckets used in simulation **5**
Number of nozzles **1**	Jet diameter **15 cm**
Bucket Dimensions	
Length (A) **34 cm**	Width (B) **32.5 cm**
Depth (C) **9.5 cm**	Bucket cutout (S) **14.5 cm**
Operating conditions	
Inlet fluid pressure **atmospheric**	Inlet fluid velocity **100 m/s**
Silt particle dia. **250 µm**	Silt concentration **0.06 kg/s** (30 ppm)
Spear Material **Carbon steel**	Transient Problem

- **Location of erosion on the buckets studied.**
  Silt particle size 250 µm, silt mass flow rate 0.01 kg/s, inlet fluid velocity 100 m/s and inlet fluid pressure - atmospheric.

5.2 Geometry

Geometries were constructed in Solidworks. The dimensions and various views of the geometries are depicted in the subsequent section.

5.2.1 Pelton turbine spear and nozzle

Figures 5.1, 5.2, 5.3 and 5.4 show the Pelton turbine nozzle geometry that has been designed for the problem. The dimensions have been taken from the work of Benzon et.al [2015] on impulse

turbine. The geometry was created in SOLIDWORKS. The four major components of the geometry are inlet, outlet, spear and nozzle opening.

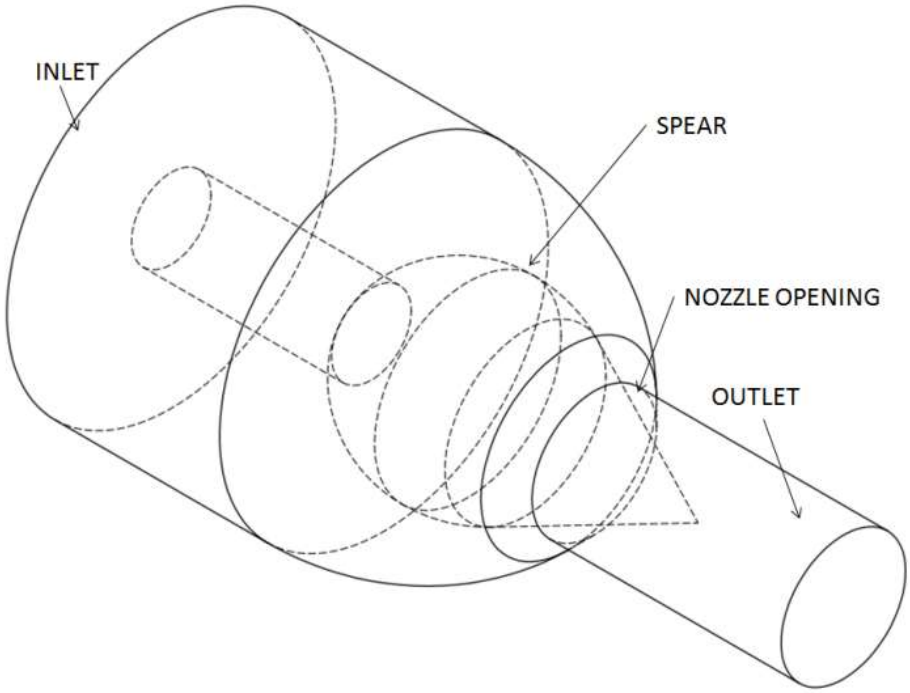

Figure 5.1: An isometric view of Pelton turbine nozzle.

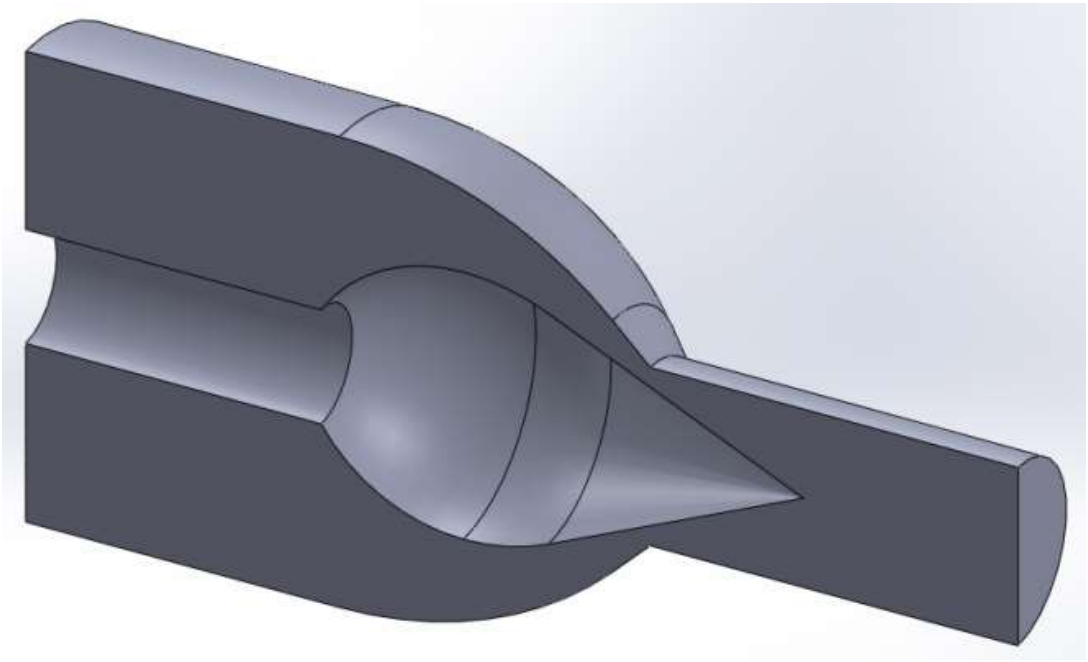

Figure 5.2: A section view of the Pelton turbine nozzle geometry.

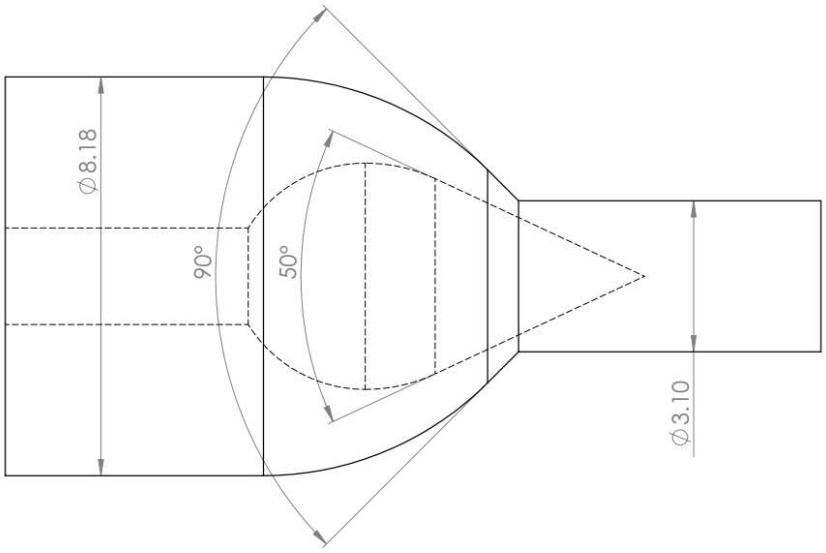

Figure 5.3: Side view of the Pelton turbine nozzle geometry (All dimensions in cm).

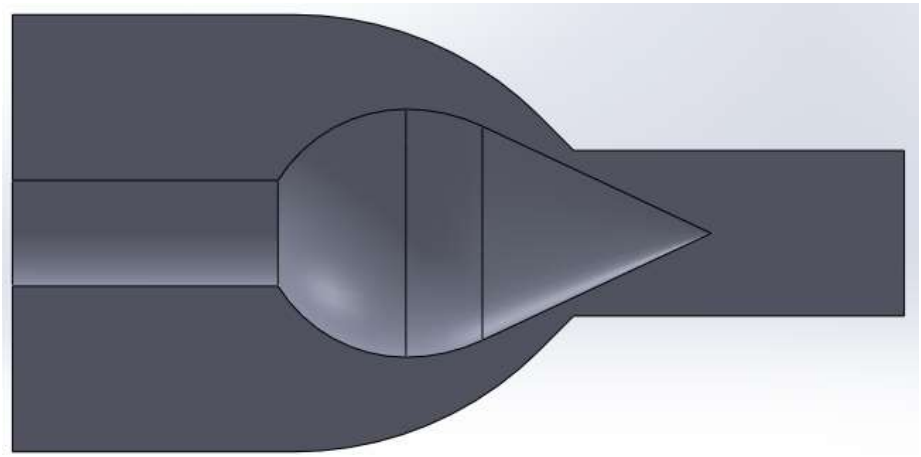

Figure 5.4: Side view of the Pelton turbine nozzle geometry (Section view).

5.2.2 Pelton turbine runner

The dimensions of the runner and bucket were calculated using correlations suggested by Dr. P. M. V. Subbarao based on jet diameter. Figures 5.5 and 5.6 show the geometry of the runner and Figs. 5.7, 5.8 and 5.9 show the geometry of the bucket. The geometry was created in SOLIDWORKS. The runner was created with only 5 blades to make the simulation easier. The side faces of the runner are treated as the outlet for the flow. The rotor was given a rotatory motion relative to the stator using mesh motion

.

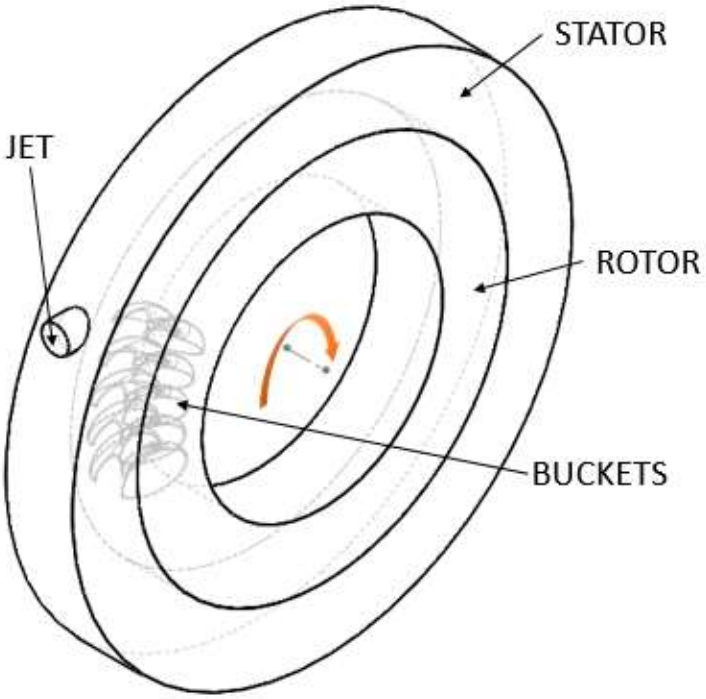

Figure 5.5: Isometric view of Pelton turbine runner.

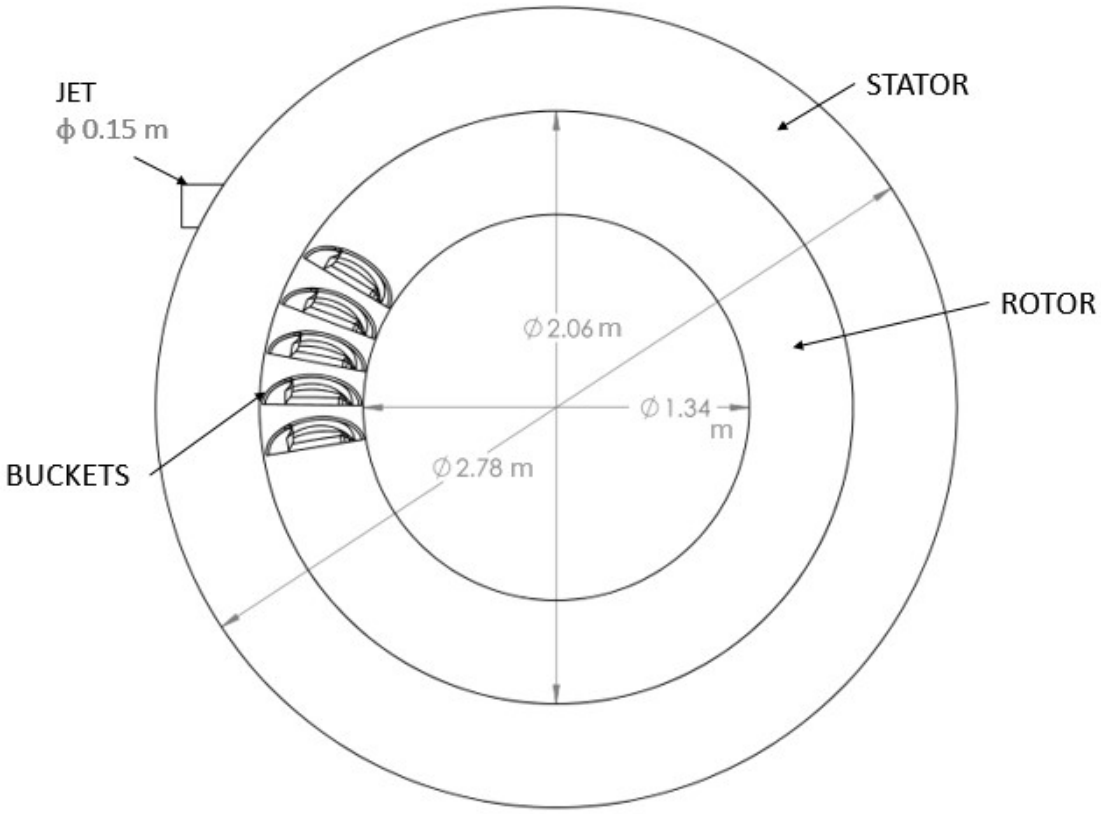

Figure 5.6: Front view of Pelton turbine runner.

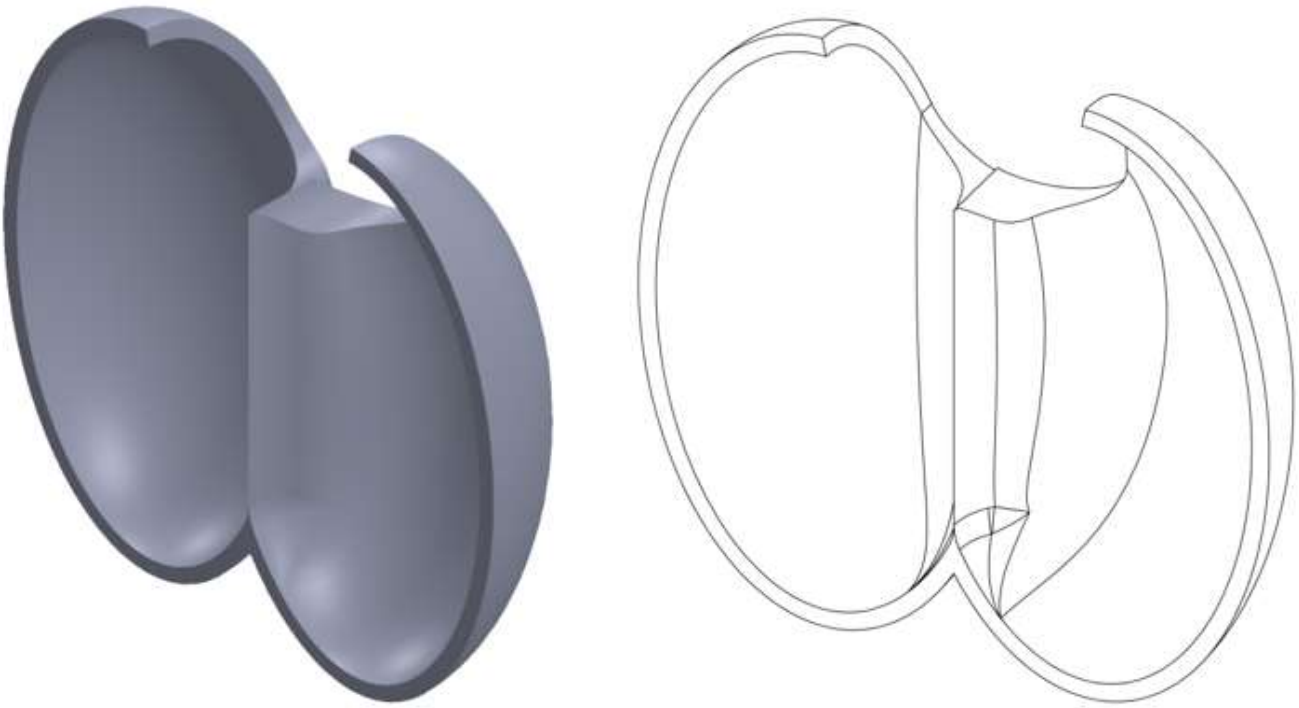

Figure 5.7: Pelton bucket isometric view rendered (left) and drawing (right).

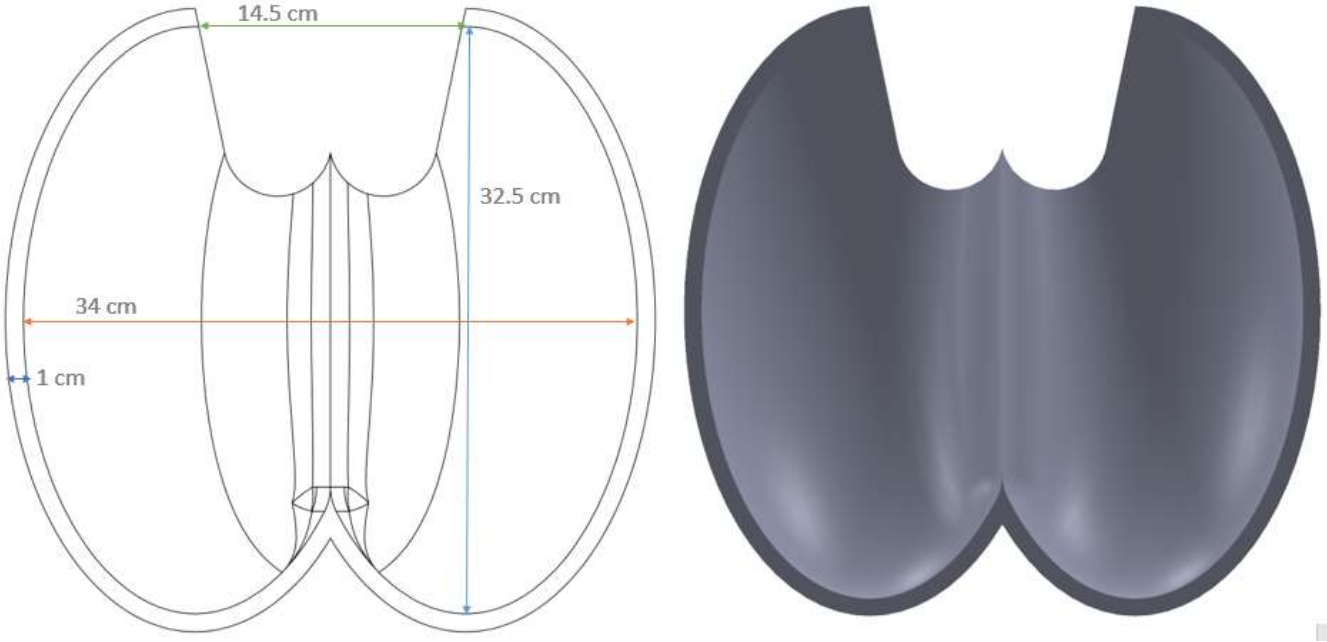

Figure 5.8: Pelton bucket front view drawing (left) and rendered (right).

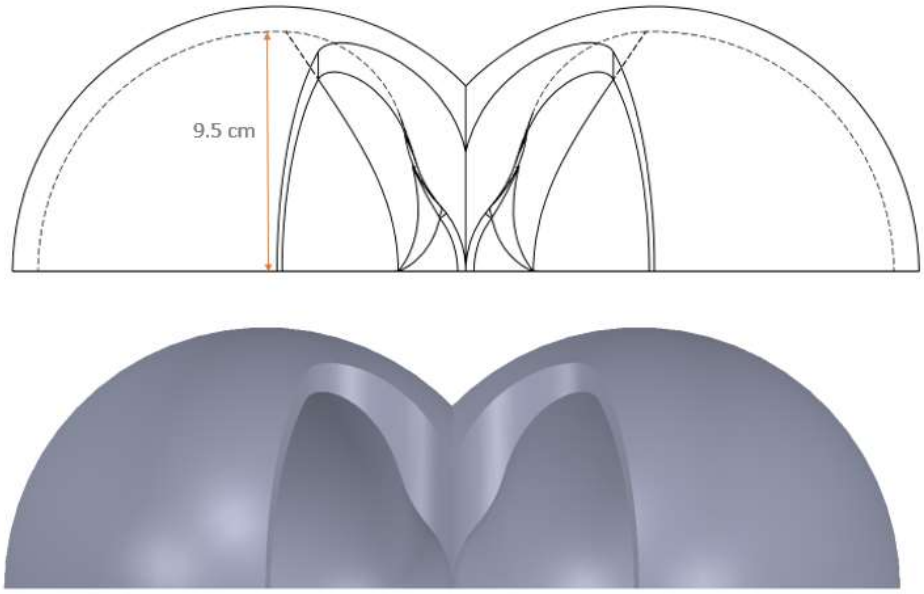

Figure 5.9: Pelton bucket top view drawing (top) and rendered (bottom).

5.3 Mesh generation

Mesh generation was done in ANSYS FLUENT's native mesh generator. Mesh was also refined to achieve grid independence.

5.3.1 Pelton turbine spear and nozzle

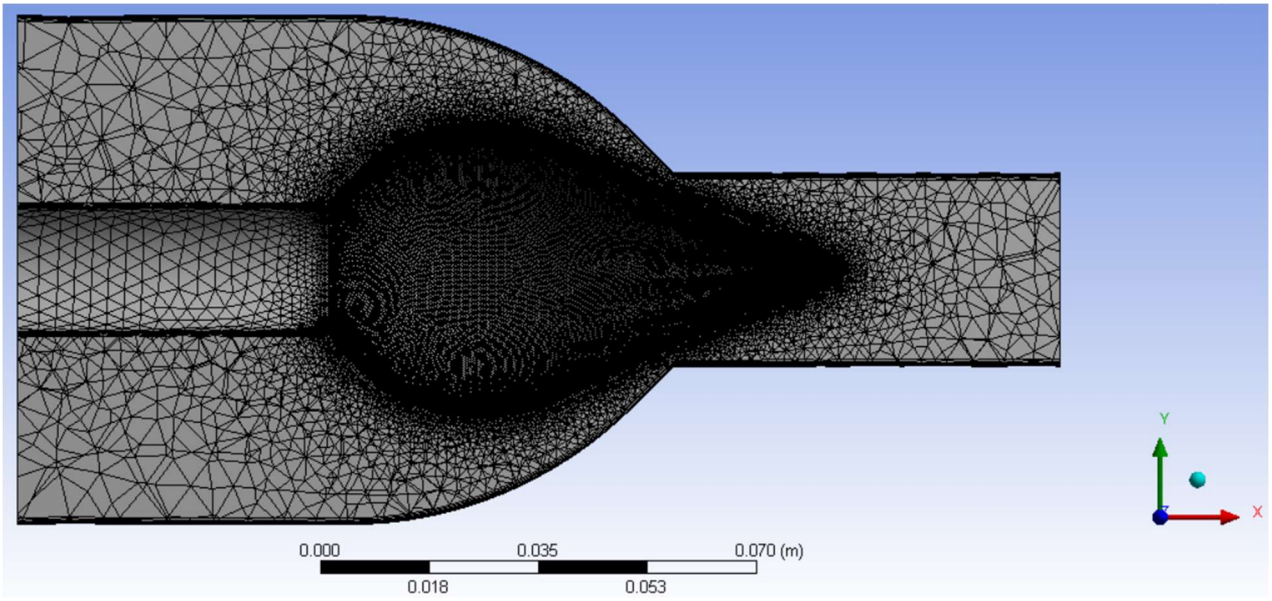

Figure 5.10: Section view of the tetrahedral mesh generated on Pelton turbine spear.

A tetrahedral mesh was generated using ANSYS FLUENT's native mesh generator (Fig. 5.10). An inflation layer at each boundary was also generated. The cells on the spear were also refined. The details of the mesh generated are listed in Table 5.3. To achieve grid convergence, the mesh was refined to 14,82,503 elements till the variations in the area weighted average of erosion rate and erosion pattern were not significant.

Table 5.3: Meshing details for the Pelton spear.

Meshing element used	Tetrahedrons		
Minimum edge length	6.2204e-2 m		
Nodes	4,35,246		
Elements	14,82,503		
Inflation layers	5 (on both boundaries)		
Inflation method	Total thickness		
Max. inflation layer thickness	1e-3 m		
Face sizing on the spear (Element size)	0.00055 m		
Orthogonal quality	Min. 0.10907	Max. 0.9999	Avg. .89405
Skewness	Min. 1.9356e-6	Max. 0.96162	Avg. 0.19874
Element quality	Min. 2.1622e-2	Max. 1	Avg. 0.76326

5.3.2 Pelton turbine runner

A tetrahedral mesh was generated using ANSYS FLUENT's native mesh generator (Fig. 5.11). The details of the mesh generated are listed in Table 5.4. To achieve grid convergence, the mesh was refined to 20,06,527 elements till the variations in the area weighted average of erosion rate and erosion pattern were not significant.

Table. 5.4: Meshing details for the Pelton turbine runner.

Meshing element used	Tetrahedrons
Min. Edge length	7.8313e-8m
Nodes	3,62,222
Elements	20,06,527

Orthogonal quality	Min. 0.20377	Max. 0.99789	Avg. 0.8653
Skewness	Min. 1.2206e-11	Max. 0.90545	Avg. 0.21251
Element quality	Min. 0.17542	Max. 1	Avg. 0.84595

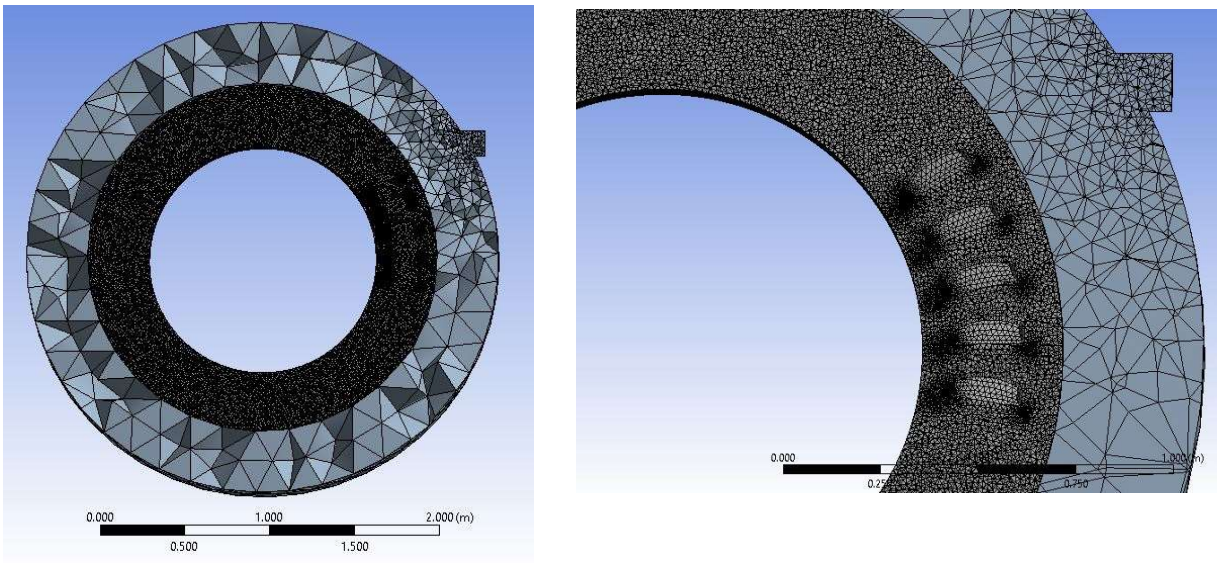

Figure 5.11 Tetrahedral mesh generated on the Pelton turbine runner.

5.4 Fluid phase and discrete phase model conditions

The standard k-epsilon (2-eqn) viscous model with scalable wall functions was used for the discrete phase.

Apart from the k-epsilon model, the discrete phase model was also turned on for simulating the silt. The following settings were enabled in the DPM model-

- '**Interaction with the continuous phase**' option enabled to calculate the erosion rate at the wall.
- '**Erosion/Accretion**' model enabled from physical laws.
- '**Number of continuous phase iteration per DPM iteration**' set to 10.
- In '**Tracking parameters**', Max. no. of tracking steps - 10000. Step length factor set to 15.
- '**Unsteady particle tracking'** was unchecked.
- An injection is set up for the silt. The following properties of the injection were defined for the Pelton spear (Table 5.5) and runner (Table 5.6):

Table 5.5: DPM injection properties for the Pelton spear.

Injection type	Surface
Release from surface	Inlet
Particle type	Inert
Material	silt (User defined)
Diameter distribution	Uniform
'Inject using face normal direction' enabled.	
Under point properties	
1. Diameter	250 µm
2. Velocity	4.4 m/s
3. Total flow rate	0.0005 kg/s

Table 5.6: DPM injection properties for the Pelton runner.

Injection type	Surface
Release from surface	Inlet
Particle type	Inert
Material	silt (User defined)
Diameter distribution	Uniform
'Inject using face normal direction' enabled.	
Under point properties -	
1. Diameter	250 µm
2. Velocity	100 m/s
3. Total flow rate	0.06 kg/s

5.5 Cell zone conditions

In '**Cell zone conditions**' the material is set to h2o-liquid for all components. For Pelton runner, rotary motion was given to the rotor part using the '**Mesh motion**' option. Mesh motion settings for Pelton rotor are shown in Table 5.7.

Table 5.7: Mesh motion settings for Pelton rotor.

Axis of rotation	X = -1, Y = 0, Z = 0
Speed of rotation	300 RPM

5.6 Boundary conditions

The inlet and outlet boundary conditions for the Pelton spear and runner are mentioned in Tables 5.8 and 5.9.

Table 5.8: Inlet and outlet boundary conditions for the Pelton spear.

AT INLET	
Velocity magnitude	4.4 m/s
Initial gauge pressure	1 MPa
AT OUTLET	
Gauge pressure	0 Pa

Table 5.9: Inlet and outlet boundary conditions for the Pelton runner.

AT INLET	
Velocity magnitude	100 m/s
Initial gauge pressure	0 Pa
AT OUTLET	
Gauge pressure	0 Pa

The DPM boundary conditions defining the behaviour of the silt particles at the wall of the geometry is as follows:

5.6.1 Boundary condition type 'reflect'

Silt particles reflect off the walls of the geometry.

5.6.2 Discrete phase reflection coefficients

Govern the reflection of particles off the wall of the geometry. Values used were for sand reflecting off of carbon steel. Values taken from the DNVGL-RP-0501 manual on 'Managing Sand Production and Erosion' [2015].

- **Normal - polynomial type**

Table 5.10: Discrete phase reflection coefficients, normal - polynomial type.

Coefficient	Value
1	0.993
2	-0.0307
3	4.75e-4
4	-2.61e-6

- **Tangent - polynomial type**

Table 5.11: Discrete phase reflection coefficients, tangent - polynomial type.

Coefficient	Value
1	0.998
2	-0.029
3	6.43e-4
4	-3.56e-6

5.6.3 Erosion model coefficients

Constants used in the erosion model depending upon the nature of the erodent and the target surface. Values used were for sand eroding carbon steel. Values taken from the DNVGL-RP-0501 manual on 'Managing Sand Production and Erosion' [2015]. Impact angle function is chosen in such a way that more erosion takes place at shallow angles where erosion of ductile materials is more.

- **Impact angle function**

Table 5.12: Impact angle function values for erosion model.

Point	Angle	Value
1	0	0
2	20	0.8
3	30	1
4	45	0.5
5	90	0.4
6	135	0.5
7	150	1
8	160	0.8
9	180	0

- **Diameter function** – constant: 1.8e-9
- **Velocity exponent** – constant: 2.6

5.7 Solution controls

1. Under relaxation factors- Pressure 0.7 Momentum 0.3

2. Convergence criterion - 10^{-3} for all parameters

3. Hybrid Initialization used.

4. For Pelton spear: Steady state simulation, No. of iterations used were 500.

5. For Pelton runner: Transient simulation,
   Time step size used was 0.0025 s
   No. of time steps used were 12
   No. of iterations per time step used were 40

5.8 Results and discussion

Figure 5.12 shows the particle tracks and the magnitude of their velocities at different locations. It can be seen from the particle tracks (Fig. 5.12) that silt particles tend to accelerate along with the flow and reach their maximum velocity (around 8 m/s) near the tip of the spear.

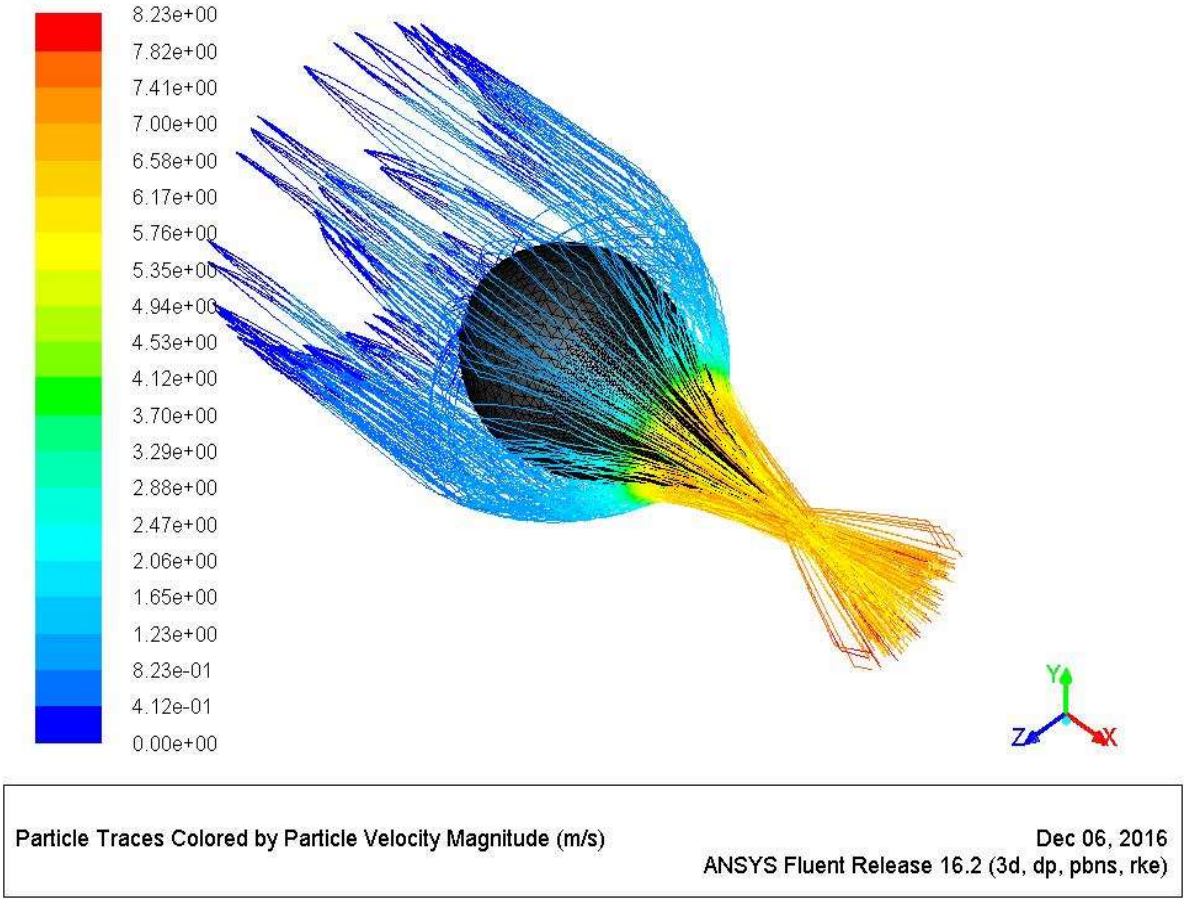

Figure 5.12: Particle tracks around Pelton spear coloured by the magnitude of velocities.

Figure 5.13 shows the eroded region in the spear with the erosion rate in terms of kg/m^2-s. Area weighted average of erosion rate for particle size of 250 µm and 0.0005 kg/s mass flow rate was found to be 0.0029543498 kg/m^2-s**.** Integral of the erosion rate over the spear surface yielded erosion rate of 2.4778927e-11 kg/s. Maximum erosion rate was found to be 0.8336133 kg/m^2-s**.**

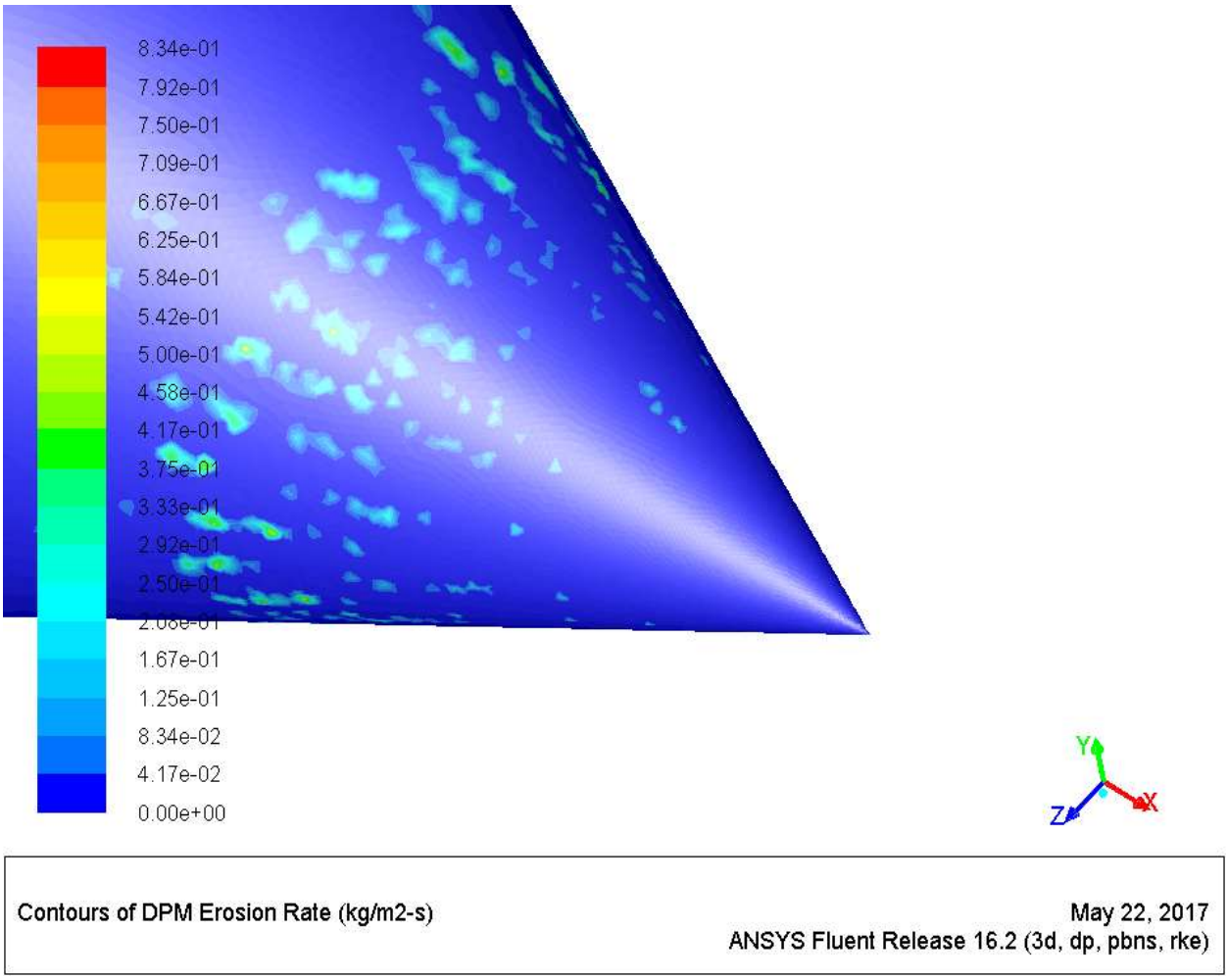

Figure 5.13: Contour of eroded Pelton turbine spear.

The erosion contour also shows heavy erosion right at the tip of the spear with a max. erosion rate of 0.8336133 kg/m^2-s. This can be explained by the high velocity of the silt particles near the tip of the spear (Fig. 5.12) and the sudden change in direction of silt particles near the nozzle opening causing them to strike the spear. The location of the wear predicted by the DPM model is also in agreement with the field observational results and literature [Chongji et al., 2014].

Figure 5.14 shows the variation of area weighted average of erosion rate with silt mass flow rate for 250 μm particle size. It is observed that the erosion rate increases with increase in the silt mass flow rate. This is in agreement with the theoretical results [Padhy and Saini, 2009].

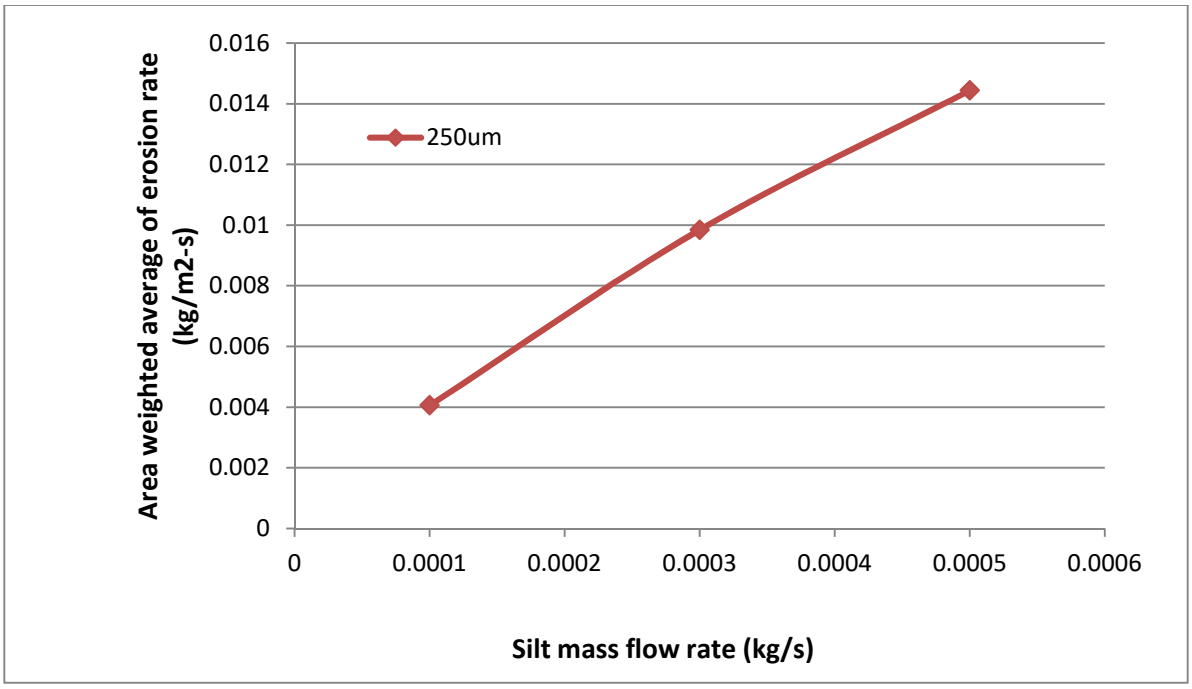

Figure 5.14: Variation of area weighted average of erosion rate with silt mass flow rate for 250 µm particle size.

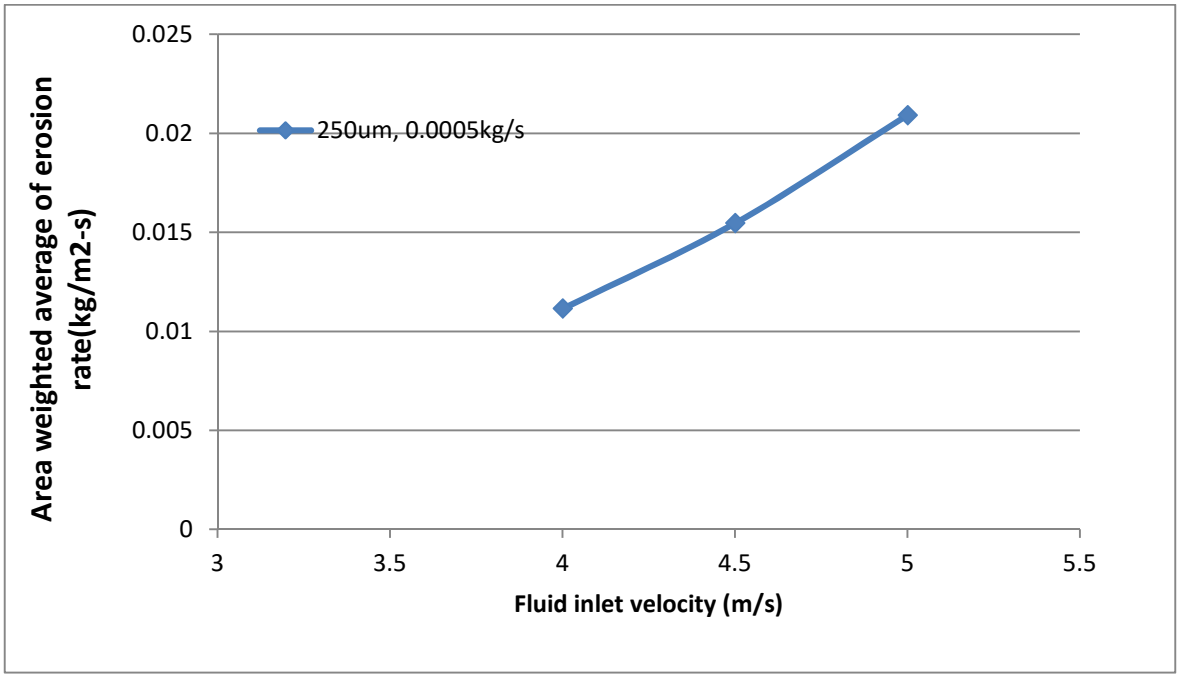

Figure 5.15: Variation of area weighted average of erosion rate with fluid inlet velocity for 250 µm particle size and 0.0005 kg/s silt mass flow rate.

Figure 5.15 shows the variation of area weighted average of erosion rate with fluid inlet velocity for 250 µm particle size and 0.0005 kg/s silt mass flow rate. Increase in the fluid inlet velocity also leads to an increase in erosion rate as predicted by the theoretical results [Khurana et al., 2012].

Figure 5.16 shows the erosion contour plot of the Pelton runner buckets. Figure 5.17 shows the position of the Pelton runner and streamlines of the jet at various time steps.

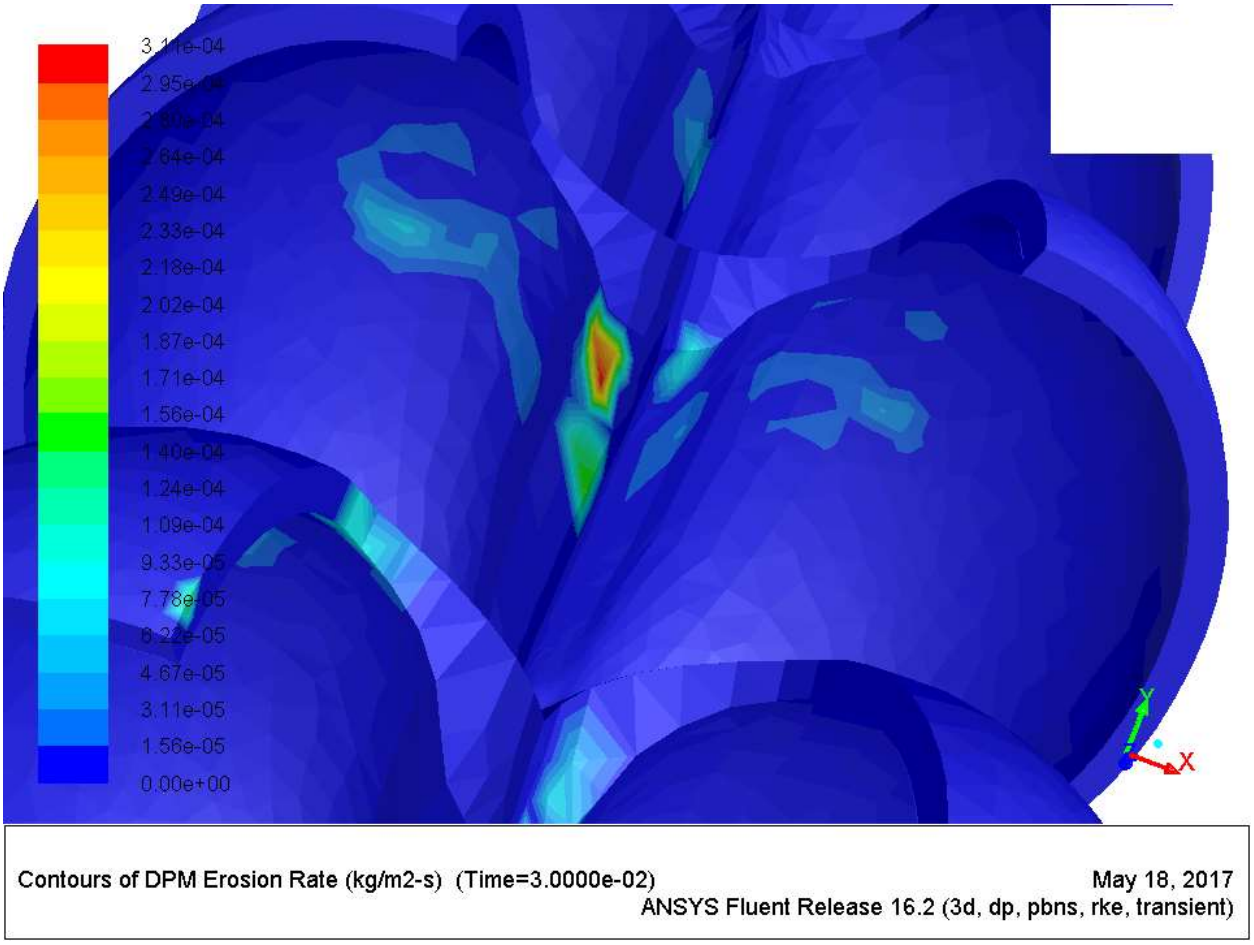

Figure 5.16: Erosion contour plot of the Pelton runner bucket.

In Pelton runner, area weighted average of erosion rate for particle size of 250 µm and 0.06 kg/s silt mass flow rate was found to be 2.697149e-7 kg/m^2-s**.** Integral of the erosion rate over the surface of the buckets yielded erosion rate of 8.4056166e-7 kg/s. Maximum erosion rate was found to be 0.0003110286 kg/m^2-s**.**

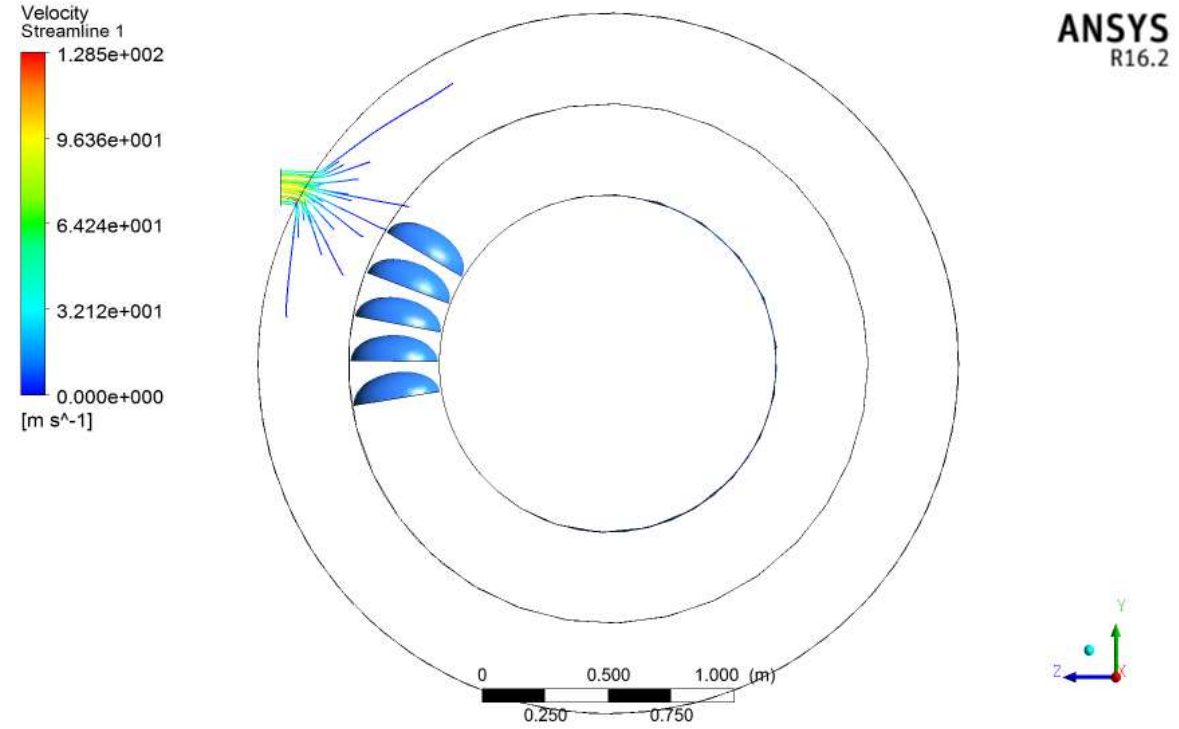

(a) Time step 0 (0 s)

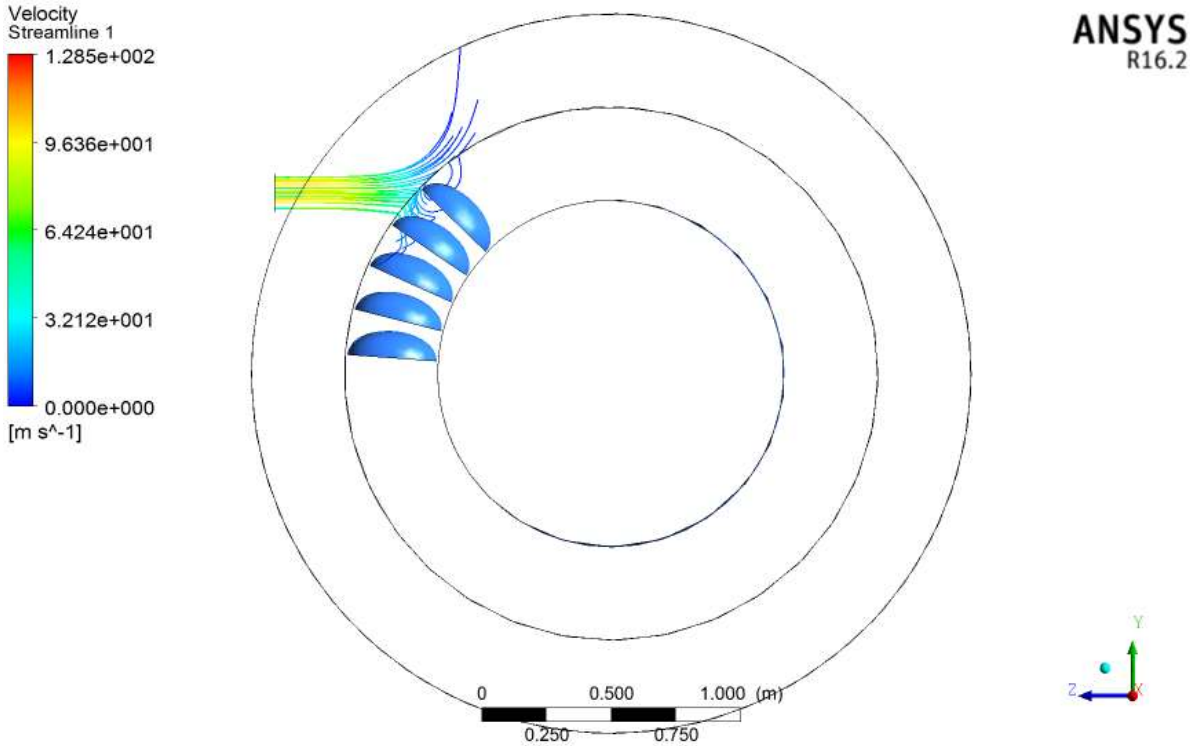

(b) Time step 3 (0.0075 s)

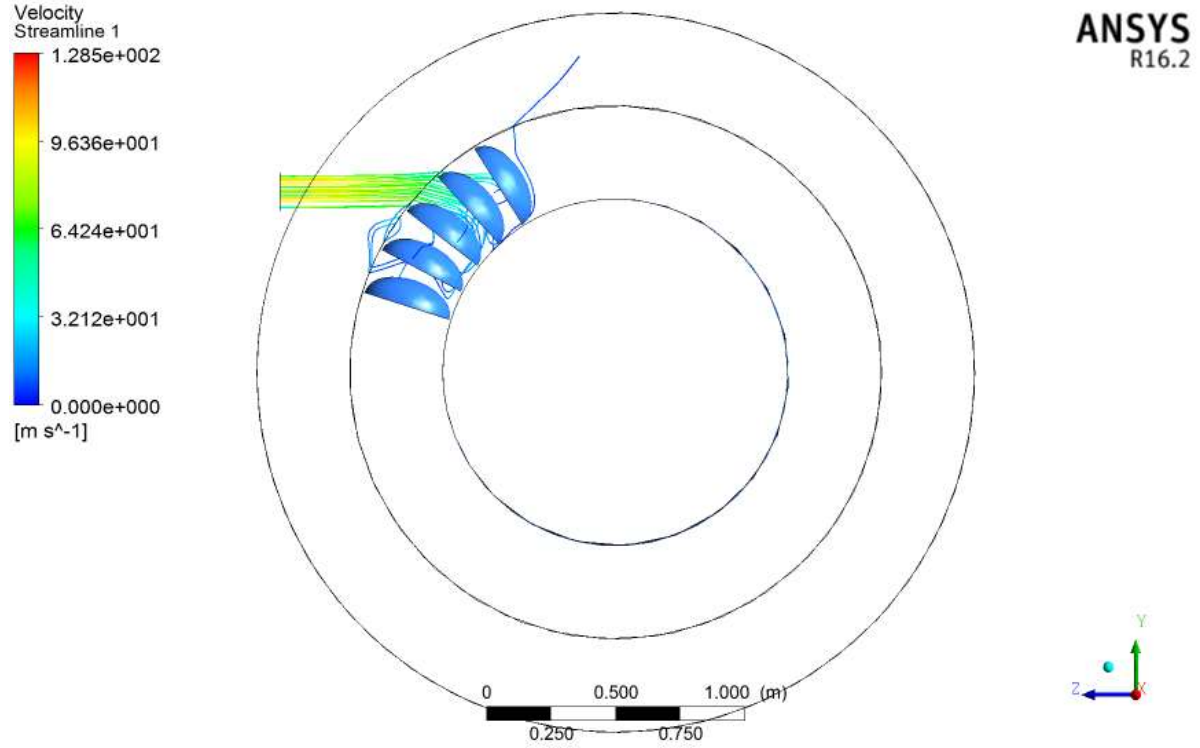

(c) Time step 6 (0.015 s)

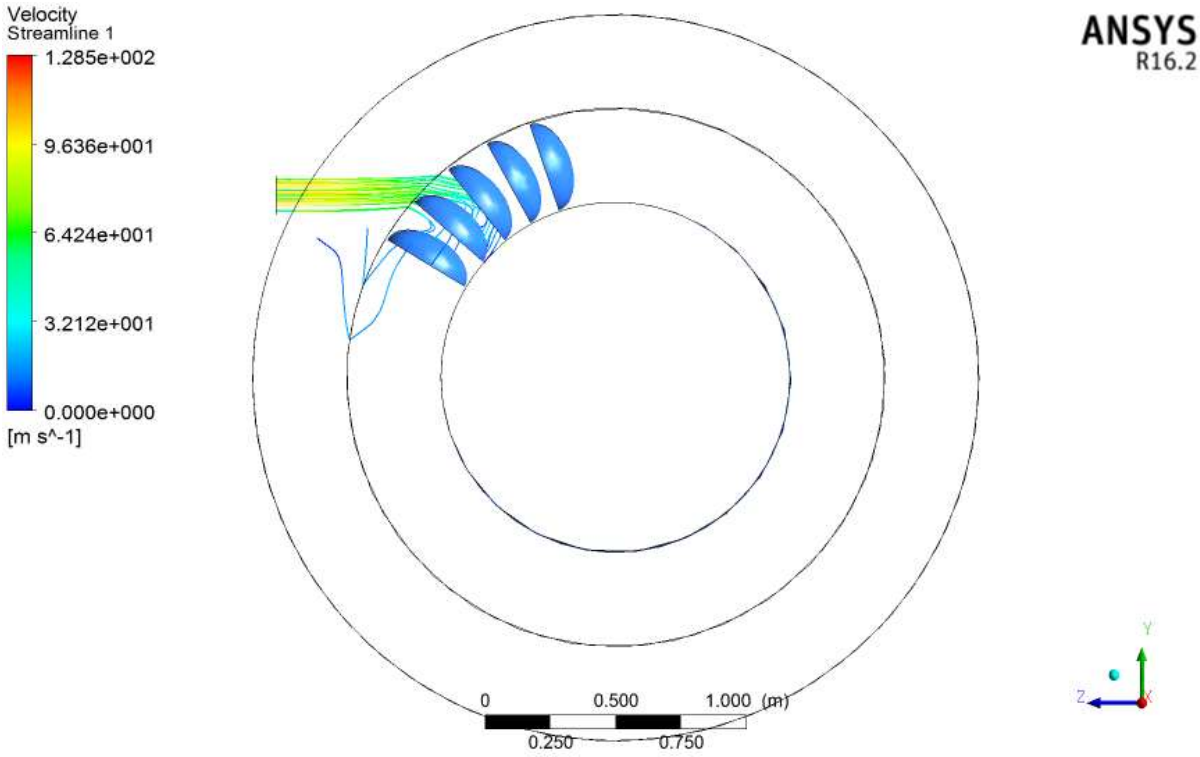

(d) Time step 9 (0.0225 s)

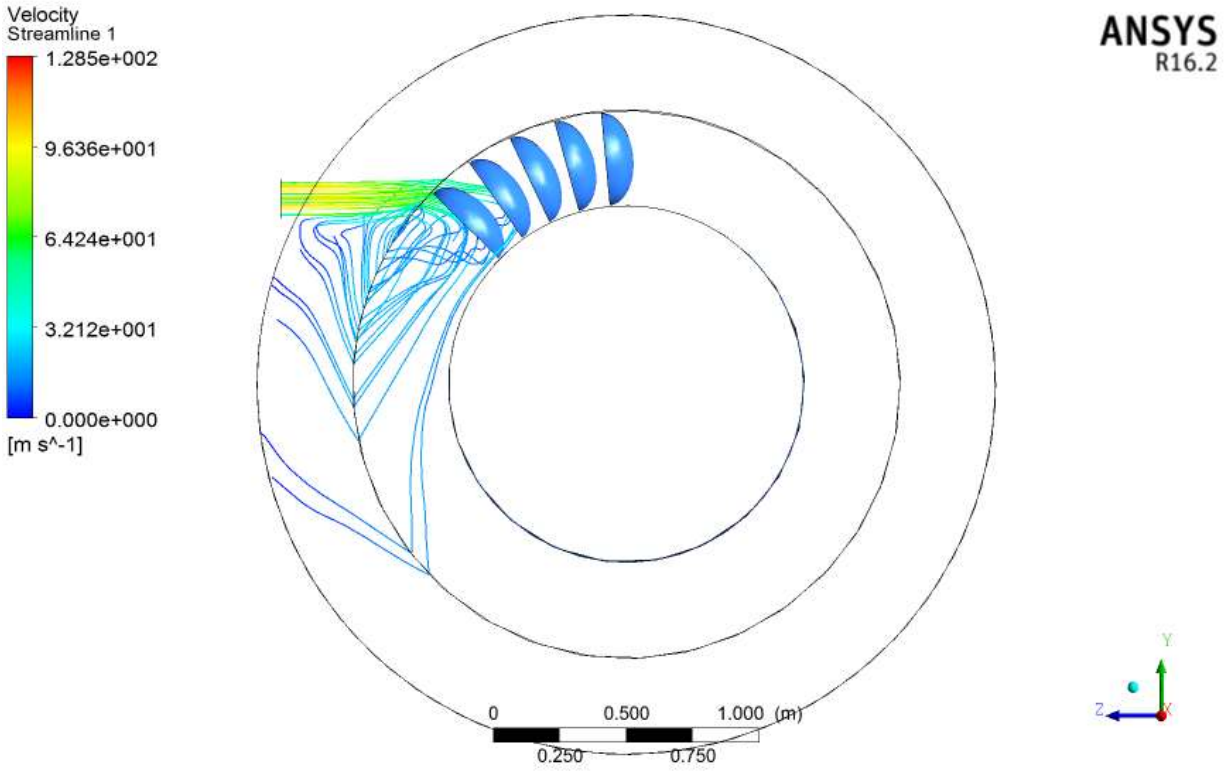

(e) Time step 12 (0.03 s)

Figure 5.17: Streamlines of the water jet and Pelton runner position at various time steps.

The erosion contour plot for the Pelton runner (Fig. 5.16) shows two main regions that are most severely affected by silt particles. First region is the splitter of the bucket. Second region is the innermost region of the bucket where the silt particles change direction. The main reason for the heavy erosion at the splitter is the fact that the water jet hits the splitter of the bucket first with a very high velocity (Fig. 5.17). More the particle impingement energy, more is the erosion. Also, when the jet along with the silt particles moves into the bucket, the sudden change of direction at the innermost region of the bucket causes the silt particles to strike the surface due to inertia. This results in the erosion shown in the inner regions of the bucket. The eroded areas predicted by the simulation are in accordance with the literature [Kumar and Saini, 2015].

Chapter 6

Conclusions

Hard surface coatings have proven to be effective in protecting hydro turbine components against silt erosion. Based on the performances in slurry pot wear test, boronized 13-4 MSS was found to be the most erosion resistant coating. However, due to the costly nature of the boronizing process and its application for small sized components only, it may not be feasible for all hydro turbine parts. HVOF coatings are much more suitable because of the standardized process, commercial acceptability and its application for large sized components. Hence, WOKA and WOKA + Y_2O_3 can be recommended for use in hydro turbines. Use of CFD simulations to predict the erosion prone areas has also proven to be successful, with results matching closely with the real world observations. The following are the conclusions from the work done in this study:

1. All the coatings WOKA, WOKA + Y_2O_3 and boronizing on 13-4 MSS substrate resulted in an improved wear resistance against silt erosion as compared to the bare steel. This is evident from the wear curve (Fig. 4.14).
2. HVOF coated cermets WOKA, WOKA + Y_2O_3 resulted in a 15% and 25% reduction in wear volume, respectively as compared to the bare 13-4 MSS steel.
3. The improved wear resistance of the HVOF coated cermets was attributed to their higher hardness (WOKA – 1050 VHN, WOKA + Y_2O_3 – 1150 VHN).
4. The addition of 2 wt% of Y_2O_3 in WOKA cermet also led to an improvement in wear resistance. A 11% reduction in wear volume was observed in WOKA + Y_2O_3 as compared to the WOKA coating.
5. The improved wear resistance of the WOKA + Y_2O_3 coating was attributed to the addition of another hard phase Y_2O_3 which resulted in increased hardness of WOKA + Y_2O_3 coating (1150 VHN).
6. Boronized 13-4 MSS exhibited superior wear resistance as compared to bare 13-4 MSS with a 50% reduction in wear volume.

7. The improved wear resistance of the boronized 13-4 MSS was attributed to its extremely high hardness of 1655 VHN.
8. On microstructural examination, the wear mechanism of 13-4 MSS was found to be by micro cutting. Hence, ductile mode of erosion was found in 13-4 MSS. In HVOF coatings, the removal of binder matrix and pulling out of WC grains was found to be the wear mechanism. The mode of erosion in HVOF coating was found to be mainly ductile. In boronized 13-4 MSS, the removal of material was due to the chipping away of the surface by the impact of silt particles. Hence, the mode of erosion was found to be brittle in the boronized steel.
9. CFD simulation of the Pelton turbine spear and nozzle revealed the tip of the spear to be the most eroded area. The high velocity of silt particles near the nozzle opening was the reason for the heavy erosion at spear tip.
10. Erosion rate predicted by the model was found to increase with the increase in silt mass flow rate and fluid inlet velocity. This result predicted by the simulation was found to be in agreement with the literature.
11. CFD simulation of Pelton turbine runner revealed the splitter and the innermost region of the buckets to be the most eroded areas. The splitter was found to be the most eroded as it takes the first impact of the high velocity water jet. The sudden change in direction at the inner regions of the bucket was found to be reason for the erosion at the bucket.
12. The eroded regions of Pelton turbine predicted by the simulation were in good agreement with the field observational results.

6.1 Scope for future work

1. Other ceramic reinforcements like vanadium carbide, chromium carbide, titanium carbide, etc. could also be added into the existing WOKA cermet in varying quantities to achieve an improvement in wear resistance.
2. Binder/matrix strength of the cermet could also be improved by addition of components like carbon nanotubes.
3. Boronized hydro turbine components could be tested in real world conditions.
4. CFD simulations for erosion in hydro turbines could be done by considering the combined effect of silt erosion, cavitation and corrosion.
5. Newer and improved erosion models could be used for future studies.

References

Benzon, D., Židonis, A., Panagiotopoulos, A., Aggidis, G.A., Anagnostopoulos, J.S. and Papantonis, D.E., 2015. Impulse turbine injector design improvement using Computational Fluid Dynamics. *Journal of Fluids Engineering*, *137*(4), pp.041106-9.

Brekke, H., Wu, Y.L. and Cai, B.Y., 2002. Design of hydraulic machinery working in sand laden water. *Abrasive Erosion & Corrosion of Hydraulic Machinery*, pp.156-171.

Callister, W.D. and Rethwisch, D.G., 2011. *Materials science and engineering* (Vol. 5). NY: John Wiley & Sons, pp.539-565.

Campos-Amezcua, A., Gallegos-Muñoz, A., Romero, C.A., Mazur-Czerwiec, Z. and Campos-Amezcua, R., 2007. Numerical investigation of the solid particle erosion rate in a steam turbine nozzle. *Applied Thermal Engineering*, *27*(14), pp.2394-2403.

Chongji, Z., Yexiang, X., Wei, Z., Yangyang, Y., Lei, C. and Zhengwei, W., 2014. Pelton turbine needle erosion prediction based on 3D three-phase flow simulation. *IOP Conference Series: Earth and Environmental Science*, 22(5), pp.052019.

Davis, J.R. ed., 2004. *Handbook of thermal spray technology*. ASM International, pp.54-77.

Fichtl, W., 1981. Boronizing and its practical applications. *Materials & Design*, *2*(6), pp.276-286.

Goyal, D.K., Singh, H., Kumar, H. and Sahni, V., 2012. Slurry erosion behaviour of HVOF sprayed WC–10Co–4Cr and Al_2O_3 + 13TiO_2 coatings on a turbine steel. *Wear*, *289*, pp.46-57.

Hutchings, I.M. and Shipway, P., 1992. *Tribology: friction and wear of engineering materials*. Butterworth-Heinemann Publications, pp.171-198.

Jain, V. and Sundararajan, G., 2002. Influence of the pack thickness of the boronizing mixture on the boriding of steel. *Surface and Coatings Technology*, *149*(1), pp.21-26.

Joshi, A.A. and Hosmani, S.S., 2014. Pack-boronizing of AISI 4140 steel: boronizing mechanism and the role of container design. *Materials and Manufacturing Processes*, *29*(9), pp.1062-1072.

Kayali, Y., Büyüksais, A. and Yalçin, Y., 2013. Corrosion and wear behaviors of boronized AISI 316L stainless steel. *Metals and Materials International*, *19*(5), pp.1053.

Khurana, S., Kumar, V. and Kumar, A., 2012. Effect of nozzle angle and silt parameters on erosion and performance of Turgo impulse turbine. *International Journal of Thermal Technologies*, *2*(4), pp.204-208.

Khurana, S. and Goel, V., 2014. Effect of jet diameter on erosion of Turgo impulse turbine runner. *Journal of Mechanical Science and Technology*, *28*(11), pp.4539-4546.

Kumar, L., Parashar, C. And Kaur, S., 2013. Prediction of silt erosion in hydraulic turbine using non linear regression model. *IJESR,* pp.963-970.

Kumar, M. and Saini, R.P., 2015. CFD analysis of silt erosion in Pelton turbine. *International Conference on Hydropower for Sustainable Development, Dehradun,* pp. 218-227.

Machio, C.N., Akdogan, G., Witcomb, M.J. and Luyckx, S., 2005. Performance of WC–VC–Co thermal spray coatings in abrasion and slurry erosion tests. *Wear*, *258*(1), pp.434-442.

Mack, R., Drtina, P. and Lang, E., 1999. Numerical prediction of erosion on guide vanes and in labyrinth seals in hydraulic turbines. *Wear*, *233*, pp.685-691.

Maiti, A.K., Mukhopadhyay, N. and Raman, R., 2007. Effect of adding WC powder to the feedstock of WC–Co–Cr based HVOF coating and its impact on erosion and abrasion resistance. *Surface and Coatings Technology*, *201*(18), pp.7781-7788.

Mann, B.S., 1997. Boronizing of cast martensitic chromium nickel stainless steel and its abrasion and cavitation-erosion behaviour. *Wear*, *208*(1), pp.125-131.

Mann, B.S., 2000. High-energy particle impact wear resistance of hard coatings and their application in hydroturbines. *Wear*, *237*(1), pp.140-146.

Mann, B.S. and Arya, V., 2001. Abrasive and erosive wear characteristics of plasma nitriding and HVOF coatings: their application in hydro turbines. *Wear*, *249*(5), pp.354-360.

Neopane, H.P., 2010. Sediment erosion in hydro turbines. Doctoral dissertation, Faculty of Engineering Science and Technology, Norwegian University of Science and Technology.

Neopane, H.P., Dahlhuag, O. and Cervantes, M., 2011. Sediment erosion in hydraulic turbines. *Global Journal of Engineering*, *9*(6).

Padhy, M.K. and Saini, R.P., 2008. A review on silt erosion in hydro turbines. *Renewable and Sustainable Energy Reviews*, *12*(7), pp.1974-1987.

Padhy, M.K. and Saini, R.P., 2009. Effect of size and concentration of silt particles on erosion of Pelton turbine buckets. *Energy*, *34*(10), pp.1477-1483.

Padhy, M.K., Thatoi, D.N. and Acharya, A.K., 2012, March. Effect of shape of silt particles on erosive wear of Pelton turbine bucket. *International Conference on Advances in Engineering, Science and Management (ICAESM),* pp.19-24.

Patel, H.N., Singal, S.K. and Saini, R.P., 2013. A new approach for the study of silt erosion of hydro turbine. *IJETAE.*

Pawlowski, L., 2008. *The science and engineering of thermal spray coatings*. John Wiley & Sons, pp.85-89.

Sangal, S., Singhal, M.K., Saini, R.P., 2016. CFD based analysis of silt erosion in Kaplan hydraulic turbine. *International Conference on Signal Processing, Communication, Power and Embedded System, IEEE.*

Subrahmanyam, J., 1982. Studies on boronising of mild steel. *Materials Letters*, *1*(3-4), pp.100-103.

Subrahmanyam, J. and Gopinath, K., 1984. Wear studies on boronized mild steel. *Wear*, *95*(3), pp.287-292.

Swarnakar, N.K., Rao, V.S. and Tripathi, S., 2008. Innovative Use of Technology to Curb the Menace of Silt Erosion in Hydro Turbines. *Water and Energy Abstracts*, *18*(1), pp.27-28.

Thakur, L. and Arora, N., 2017. A study of processing and slurry erosion behaviour of multi-walled carbon nanotubes modified HVOF sprayed nano-WC-10Co-4Cr coating. *Surface and Coatings Technology*, *309*, pp.860-871.

Thapa, B.S., Thapa, B. and Dahlhaug, O.G., 2012. Empirical modelling of sediment erosion in Francis turbines. *Energy*, *41*(1), pp.386-391.

Wilson, K., Stack, M.M. and Abdelrahman, S.M., 2011. A CFD model of particle concentration effects on erosion–corrosion of Fe in aqueous conditions. *Wear*, *273*(1), pp.38-42.

Web References

Annual Report 2008-2009, powermin.nic.in/sites/default/files/uploads/Annual_Report_2008-09_English.pdf, (accessed on – 23/07/2016).

Discrete Phase Modelling - FLUENT User Guide, https://www.ansys.com, (accessed on - 23/07/2016).

DNVGL-RP-0501 manual on 'Managing Sand Production and Erosion', https://www.dnvgl.com/oilgas/download/dnvgl-rp-O501-managing-sand-production-and-erosion.html, (accessed on - 18/01/2017).

Publications

Conference paper

Title – "**Development of Erosion Resistant Cermet Coatings for Hydro Turbine Blades"**

Authors – **Gaurav Nath*** and **Dr. Satish Kumar**

*presenting author

Paper accepted for oral presentation at the **9th International Conference on Materials for Advanced Technologies 2017 (ICMAT 2017)** to be held at **Suntec, Singapore** from **June 18 to June 23 2017.** Conference organized by **Materials Research Society (MRS), Singapore.**

Journal paper

Title – "**Studies on Slurry Erosion Behavior of HVOF Applied Y_2O_3 Added WC-10Co-4Cr Cermet on 13-4 Martensitic Stainless Steel"**

Authors – **Gaurav Nath** and **Dr. Satish Kumar**

Under review by "**Journal of Coatings Technology and Research"** – Springer publications.